

Wafer-Scale Integration of Graphene-Based Photonic Devices

Marco A. Giambra,[†] Vaidotas Mišeikis,[†] Sergio Pezzini, Simone Marconi, Alberto Montanaro, Filippo Fabbri, Vito Soriano, Andrea C. Ferrari, Camilla Coletti,^{*,‡} and Marco Romagnoli^{*,‡}



Cite This: <https://dx.doi.org/10.1021/acsnano.0c09758>



Read Online

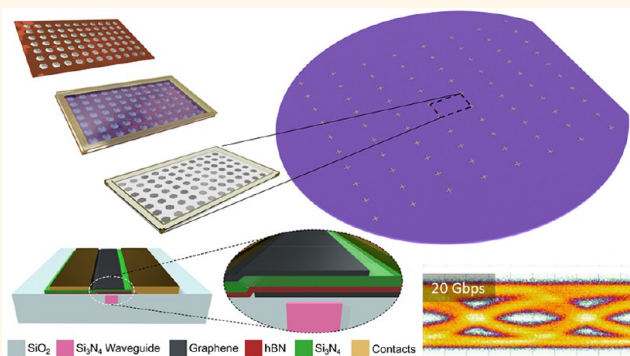
ACCESS |

Metrics & More

Article Recommendations

ABSTRACT: Graphene and related materials can lead to disruptive advances in next-generation photonics and optoelectronics. The challenge is to devise growth, transfer and fabrication protocols providing high ($\geq 5000 \text{ cm}^2 \text{ V}^{-1} \text{ s}^{-1}$) mobility devices with reliable performance at the wafer scale. Here, we present a flow for the integration of graphene in photonics circuits. This relies on chemical vapor deposition (CVD) of single layer graphene (SLG) matrices comprising up to ~ 12000 individual single crystals, grown to match the geometrical configuration of the devices in the photonic circuit. This is followed by a transfer approach which guarantees coverage over $\sim 80\%$ of the device area, and integrity for up to 150 mm wafers, with room temperature mobility $\sim 5000 \text{ cm}^2 \text{ V}^{-1} \text{ s}^{-1}$. We use this process flow to demonstrate double SLG electro-absorption modulators with modulation efficiency $\sim 0.25, 0.45, 0.75, 1 \text{ dB V}^{-1}$ for device lengths $\sim 30, 60, 90, 120 \mu\text{m}$. The data rate is up to 20 Gbps. Encapsulation with single-layer hexagonal boron nitride (hBN) is used to protect SLG during plasma-enhanced CVD of Si_3N_4 , ensuring reproducible device performance. The processes are compatible with full automation. This paves the way for large scale production of graphene-based photonic devices.

KEYWORDS: graphene, photonics, wafer scale, modulators, integration, encapsulation



INTRODUCTION

Graphene is ideally suited for photonics and optoelectronics,^{1–4} in particular, for optical⁵ and data communications,^{2,5,6} including virtual Internet servers and data centers.² In 2020, the global IP data traffic, mostly through cloud and data centers, was in the range of several zettabytes (ZB),⁷ *i.e.*, $>10^{21}$ bytes exchanged in one year. The connection of an ever-increasing number of people and things to the Internet (Internet of things, IoT⁸) is pushing the requirements in terms of bandwidth (BW), defined as amount of data exchanged per unit time,⁹ and the energy consumed by a device to exchange one bit of information.¹⁰ By 2023, >27 billion devices are expected to be connected.⁷ COVID-19 has forced people to stay at home, working and learning remotely as never before.¹¹ This resulted in an increase by 20–100% of the fixed residential network¹¹ and 10–20% change in traffic levels on the mobile network.¹¹ Thus, there is a renewed demand of traffic for applications, such as teleconferencing, video streaming, and online games.¹² Photonic technologies play a key role to satisfy these requirements. Photonic devices for next-generation telecom and datacom networks require >100

Gbps BW per single lane,¹³ a small footprint ($< \text{mm}^2$),¹⁴ a low loss of optical power within the device due to optical coupling ($< 1 \text{ dB}$),¹⁵ propagation loss $< 2 \text{ dB cm}^{-1}$,¹⁶ insertion loss (IL), *i.e.* power loss due to insertion of a device,¹⁷ $< 5 \text{ dB}$,^{18,19} low energy cost $< 1 \text{ mW/GHz}$ or, equivalently, $< 1 \text{ pJ/bit}$,^{20,21} and low cost of manufacturing ($< \$10/\text{Gbps}$ in 2020,² decreasing to $< \$1/\text{Gbps}$ by 2025).²² For these reasons, photonic devices based on alternatives to the established silicon on insulator, SOI,²³ and InP technologies are being investigated.²⁴ Silicon photonics (SiPh) modulators for ≥ 30 Gbaud applications have IL $\sim 2\text{--}3 \text{ dB}$ higher than InP- and LiNbO_3 -based modulators,²⁵ because of the free carrier effect,²⁶ requiring device lengths in the mm scale. The baud represents the data

Received: November 20, 2020

Accepted: January 21, 2021

in a transmission channel. It is a symbol that contains a string of “ n ” bits.²⁷ Typically, in optical communication systems “ n ” is 1 to 6.²⁷ The bit rate is defined as baud rate times “ n ”.^{17,27}

More compact and energy efficient devices were demonstrated exploiting resonant structures, *e.g.*, microring resonators,²⁸ or the Franz–Keldysh effect in Si–Ge alloys.²⁹ However, these have intrinsic wavelength selectivity.²⁹ InP technology provides modulators with size similar to SiPh,³⁰ large BW (>50 GHz),³¹ but with a higher cost of manufacturing,³¹ due to the greater cost of InP wafers with respect to Si ones.^{14,32,33}

Graphene-based photonics is very promising, as graphene is fully compatible with SiPh,² it has electro-absorption^{2,34} and electro-refraction properties,^{2,34} and it can be used for light modulation² and photodetection.^{1,3} The linear gapless energy-momentum relation of the massless Dirac Fermions in single-layer graphene (SLG) leads to high mobility at room temperature (RT) ($\mu > 100000 \text{ cm}^2 \text{ V}^{-1} \text{ s}^{-1}$)^{35–40} and pronounced (more than 1 order of magnitude)^{35–38} ambipolar electric field effect,⁴¹ such that the surface conductivity, σ , can be tuned by applying a gate voltage.⁴¹ The tuning of σ influences the optoelectronic properties of SLG.^{42,43} σ is a complex quantity, affecting both absorption and refraction of light interacting with SLG.⁴² When SLG is placed on a waveguide (WG) core, the guided light interacts with SLG, allowing a much larger absorption with respect to normal incidence.⁴⁴ The absorption coefficient for SLG on a SOI WG is up to $0.1 \text{ dB } \mu\text{m}^{-1}$,⁴⁵ depending on SLG doping⁴⁵ and distance from the WG core center.⁴⁶

SLG has been used for electron absorption^{46,47} and electron refraction modulation,^{48,49} switching,⁵⁰ and photodetection.^{1–3,51–55} Reference 46 reported electron absorption modulators (EAMs) based on SLG transferred on a 7 nm Al_2O_3 layer deposited on a Si WG. This configuration was improved by using a SLG-insulator-SLG stack, *i.e.*, a double SLG (DSLGL),² on an undoped Si WG.^{45,47,56} This has two main advantages: (1) the use of a passive WG platform, *i.e.*, pure dielectric WGs, without implantation or epitaxy processes typically employed in SiPh^{57,58} or InP,³¹ simplifying the manufacturing process, with a consequent cost reduction; (2) enhanced modulation due to the interaction of two SLGs with the WG mode.³⁴ Single-mode WGs have typical dimensions which depend on the refractive index of the guiding material.⁵⁹ SiPh single-mode WGs, guiding only the fundamental mode,⁵⁹ have a typical width $\sim 480 \text{ nm}$ when realized on 220 nm SOI.⁶⁰ Si_3N_4 single-mode WGs have larger width $\sim 1 \mu\text{m}$, depending on Si_3N_4 thickness,³⁹ because of the lower refractive index ($n = 1.98$ for Si_3N_4 ³⁹ compared to 3.47 for Si at 1550 nm).⁶¹ The larger width of Si_3N_4 WGs helps simplify the technology because it requires less stringent lithography resolution and also reduces costs, making small (~ 10000 pieces/year) and medium (~ 100000 – 1000000 pieces/year) production volumes more affordable than in SOI or InP manufacturing lines.³¹ This means that the volume (*i.e.*, number of chips) threshold to implement a product in a Si fab can be reduced by using Si_3N_4 . This enables the cost-effectiveness of medium-volume products (~ 10000 – 100000 chips per year),² thus opening medium-volume markets (*e.g.*, long haul telecom systems).²

To reach a high technology-readiness level (TRL > 8, *i.e.*, system complete and qualified),⁶² adequate for photonic device production, scalable techniques for SLG growth and transfer are needed. Chemical vapor deposition (CVD) on Cu

yields SLG that, when encapsulated in hexagonal boron nitride (hBN), has electronic and structural quality (defect density, scattering time, and μ) comparable to exfoliated SLG.^{35,37,38,63} There has been significant progress for SLG scalable growth on dielectrics, such as SiO_2 ⁶⁴ and Al_2O_3 ,⁶⁵ and on CMOS-compatible Ge,^{66–68} but with RT μ limited to $\sim 2000 \text{ cm}^2 \text{ V}^{-1} \text{ s}^{-1}$.⁶⁵ Hence, as of 2020, the most common approach to obtain $\mu > 5000 \text{ cm}^2 \text{ V}^{-1} \text{ s}^{-1}$ is to transfer SLG grown on Cu to the target substrate.⁶⁹ The so-called “wet” transfer^{70,71} typically involves chemical etching Cu to release SLG.^{69,72} Alternatively, SLG can be released from the growth substrate electrochemically^{73,74} or by oxidizing Cu at the SLG interface.⁷⁵ The released SLG is then directly picked up from the aqueous solution using the target wafer, with alignment accuracy $\geq 1 \mu\text{m}$.⁷⁶ Wet-transferred SLG has $\mu \sim 10^3 \text{ cm}^2 \text{ V}^{-1} \text{ s}^{-1}$,⁶⁹ which can be improved by 2 orders of magnitude by hBN encapsulation.³⁷ “Fully dry” transfer³⁵ is based on direct pick-up of SLG from Cu using exfoliated flakes of hBN or other layered materials (LMs), such as WSe_2 .³⁹ In this approach, SLG is released from Cu and encapsulated without contact with water or solvents,³⁵ resulting in $\mu > 3 \times 10^5 \text{ cm}^2 \text{ V}^{-1} \text{ s}^{-1}$ at RT.³⁹ Thus far, scalability is limited by the size of exfoliated hBN flakes (up to $\sim 100 \mu\text{m}$),⁷⁷ but CVD hBN or amorphous BN could be used in future to solve this. The “semi-dry” approach consists in SLG delamination from Cu in an aqueous solution either electrochemically⁷⁶ or by Cu oxidation,⁷⁸ followed by lamination on the target substrate in dry conditions. This yields μ as high as in “fully dry” transfer after hBN encapsulation³⁸ while allowing scalability.⁷⁶

Here, we implement an aligned semidry transfer of SLG, based on electrochemical delamination in NaOH, and subsequent handling of a suspended polymer/SLG membrane using a frame. This approach avoids the contact of the target substrate with the aqueous solution and allows deterministic placement of SLG single crystals (SC) with $\sim 1 \mu\text{m}$ precision in the X and Y plane, thanks to a transfer setup equipped with micrometric actuators. We use a freestanding carrier membrane, comprising 2 polymer layers. This enables semidry transfer of large SLG matrices (up to ~ 12000 SLG-SCs) with coverage >80% of the target photonics device area, and integrity in terms of SLG continuity.

We report wafer-scale fabrication of DSLGL EAMs on Si_3N_4 WGs based on a stack of two SLGs separated by $\sim 17 \text{ nm}$ Si_3N_4 . We report 30 EAMs, on 4 chips from the same wafer, with uniform performance $\pm 10\%$, demonstrating wafer-scale scalability and reproducibility of the complete process. We use monolayer (1L) CVD-hBN for SLG encapsulation, to protect SLG during Si_3N_4 deposition by plasma-enhanced CVD (PECVD). We get a contact resistance $\sim 500 \Omega \mu\text{m}$ for $E_F > 0.2 \text{ eV}$, allowing us to achieve a cutoff frequency, *i.e.*, the frequency at which energy flowing through the system is reduced rather than passing through,¹⁷ $\sim 4 \text{ GHz}$ for 120 μm EAMs, and $\sim 12 \text{ GHz}$ for 30 μm ones. The operation speed is $\sim 20 \text{ Gbps}$, the highest to date in Si_3N_4 without using resonating devices. Higher speeds have only been demonstrated in Si_3N_4 with resonating devices. For example, SLG on Si_3N_4 modulators working up to 22 Gbps were reported on microring resonators,⁵⁶ while up to 40 Gbps was demonstrated by using piezoelectric lead zirconate titanate (PZT) thin films on Si_3N_4 microring resonators.⁸⁰ Because of the gapless nature of SLG,^{1–3,81} SLG photonics can operate at any wavelength, unlike refs 56 and 80, which were limited to the specific resonant wavelength.

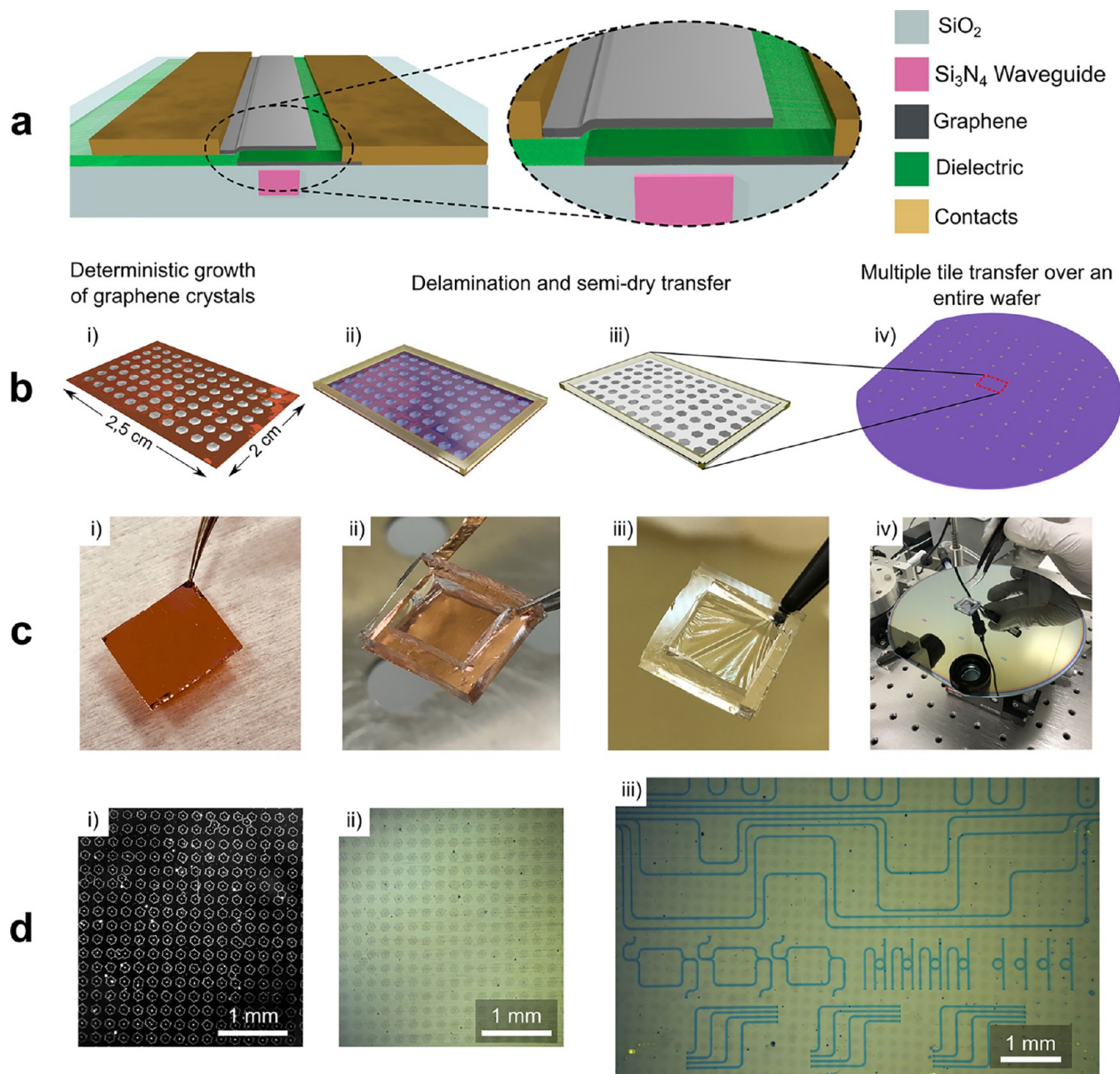


Figure 1. (a) Schematic cross-section of DSLG EAM. (b) Multiple tile stamping: (i) schematic of SC-SLG matrix on Cu, (ii) SC-SLG matrix on Cu covered with freestanding membrane and a frame, enabling aligned transfer, (iii) delaminated SC-SLG matrix with freestanding membrane and frame, (iv) transferred SLG on target wafer. (c) Photos of: (i) as-grown SLG on Cu, (ii) Cu with PDMS frame attached, (iii) suspended polymer/SLG membrane and 150 mm photonic wafer with laminated SLG. (d) Optical micrographs of (i) SC-SLG on Cu by dark field imaging, (ii) suspended SLG-SCs on polymer membrane and (iii) transferred SLG SC matrix on target wafer with photonic circuits.

RESULTS AND DISCUSSION

Our DSLG EAMs comprise two SLGs on a passive Si_3N_4 WG, separated by a ~ 17 nm Si_3N_4 dielectric, **Figure 1a**. Three factors ensure scalable fabrication with reproducibility: (i) wafer-scale source material with crystal size comparable to that of single devices, to avoid grain boundaries; (ii) semidry transfer with low impact on SLG cleanliness and electrical properties; (iii) SLG protection prior and during dielectric deposition. In ref 76, we addressed (i) by preparing SLG SC matrices. This approach is compatible with the requirements of integrated photonics, allowing tailored growth of SLG according to the geometry of the photonic circuits. The lateral

dimensions of the SLG SCs can be tuned from tens to hundreds of micrometers.^{45,56,82} Deterministic growth relies on pretreating Cu by electropolishing, to reduce surface contaminations and improve surface flatness. Cu is then patterned with 5 μm Cr seeds at the desired SLG crystal locations. This is done by using optical lithography and thermal evaporation of 25 nm Cr. The growth is performed in a cold-wall CVD reactor (Aixtron BM Pro) at 1060 $^\circ\text{C}$ by using Ar annealing to maintain a low nucleation density (~ 10 crystals per mm^2).⁷⁹ Due to residual oxidation in Cu, SLG nucleation requires surface impurities,⁸³ ensuring that SLG SCs nucleate only at the Cr seeds locations. The matrices of SLG SCs grown on Cu need to be released from the growth

substrate and transferred to the target wafer (e.g., a wafer containing WGs). To do so, we adapt our semidry transfer procedure⁷⁶ and build a dedicated transfer tool. To facilitate handling, SLG is coated with a polymer carrier membrane, and a semirigid polydimethylsiloxane (PDMS) frame is attached to the Cu foil perimeter. The transfer itself consists of two stages: (1) wet SLG electrochemical delamination from the growth substrate and (2) dry SLG aligned lamination on the target substrate. After the SLG electrochemical release from Cu in NaOH (see the [Methods](#) for details), the SLG/polymer membrane is rinsed several times in deionized (DI) water and dried in air. The freestanding membrane is supported by the PDMS frame and can be handled in dry conditions. The SLG SCs are attached to the membrane holder of the lamination tool, which allows angle adjustment with $\sim 0.1^\circ$ precision of the membrane with respect to the target wafer. The latter is brought in close proximity ($\sim 500 \mu\text{m}$) to the membrane using a 4-axis micrometrical stage (X, Y, Z translation and Θ rotation). After aligning the SLG-SCs to the photonic structures, the target wafer is heated to $\sim 100^\circ\text{C}$ and brought into contact with SLG, resulting in adhesion with the target photonics chip over the whole membrane. The alignment is performed using a 12 \times zoom microscope lens attached to a Digital single-lens reflex (DSLR) camera. The PDMS frame is then detached from the sample, and placed in acetone for the polymer removal.

During the delamination of SLG from Cu and alignment to the target substrate, the freestanding polymer-SLG membrane is supported by a semirigid frame attached to the perimeter of the sample, [Figure 1c](#). In ref [76](#), the frame was made from polyimide (Kapton) tape and bonded to the sample using an adhesive, with the risk of chemical reaction with the NaOH electrolyte contaminating the transferred SLG. To mitigate this, here we use PDMS-based support frames, which can be bonded to flat surfaces without any adhesive, thus ensuring transfer cleanliness. An alternative could be to use a solid PDMS stamp,⁸⁴ which may also handle SLG. However, PDMS is not compatible with the lamination temperature (105°C), due to its large ($\sim 3.1 \times 10^{-4} \text{K}^{-1}$) thermal expansion coefficient.⁸⁵ SLG-SCs attached to a PDMS stamps can develop nanometer-sized cracks when heated to 100°C . Our method also relies on a bilayer carrier polymer comprising 1.5 μm poly(propylene carbonate) (PPC) and 100 nm PMMA, instead of the PMMA support of ref [76](#). The different glass transition temperatures, T_G , of PPC (37°C)⁸⁶ and PMMA (105°C)⁸⁶ allow us to have a membrane with variable mechanical properties, which can be controlled with T . At ambient T , during delamination and SLG SC alignment, both polymers are kept $<T_G$, thus providing a rigid support to the freestanding membrane and preventing SLG damage. When the SLG SCs are aligned to the required position on the target wafer, SLG can be laminated on the substrate by heating to $\sim 100^\circ\text{C}$, well above the PPC T_G . The relatively thick and viscous PPC layer compared to PMMA allows the membrane to attach to the wafer and conform to surface structures, such as metal contacts, while retaining the integrity due to the solid, yet thin ($\sim 100 \text{nm}$), PMMA layer, still below the PMMA T_G . Crucially, in the lamination stage, the target substrate does not come into contact with an aqueous solution. Therefore, the transfer can be repeated on different areas of the same wafer, without risk of SLG delamination or increased contamination.

This enables the growth of SLG on a smaller scale, with greater control of strain and doping, than that currently

achievable^{87,88} when performing growth and transfer on full 150 or 200 mm wafers. The target wafer can then be populated via several transfers, as shown schematically in [Figure 1b](#). Before each SLG transfer, photonics WGs are prepared by rinsing the chip in acetone and 2-propanol, followed by a deep cleaning in a resist remover (AR-600 71) for 2 min. Following SLG transfer on the WGs, the fabrication of the DSLG stack is performed as follows. SLG is patterned and etched using electron-beam lithography (EBL) (Zeiss Ultra Plus) and reactive ion etching (RIE) (Sistec). The bottom SLG contacts are deposited via thermal evaporation of Ni/Au. A protective 1L-hBN film is transferred over the whole chip area using the semidry procedure described above.

A 17 nm Si_3N_4 gate dielectric is deposited over the whole area. Si_3N_4 is chosen over other dielectrics, such as Al_2O_3 , HfO_2 , or hBN, due its high breakdown field ($>10 \text{MV cm}^{-1}$).⁸⁹ PECVD can be used to deposit uniform Si_3N_4 with thickness $<20 \text{nm}$ and root mean square (RMS) roughness $<0.5 \text{nm}$.⁸⁹ Top SLG SCs are then placed using aligned semidry transfer. The top structure of the modulator is fabricated using identical methods to the bottom layer (see the [Methods](#) for details).

The SLG crystals are characterized throughout the fabrication process by Raman spectroscopy with a Renishaw InVia at 532 nm, laser power $\sim 1 \text{mW}$, and acquisition time $\sim 4\text{s}$. The laser spot size is $\sim 0.8 \mu\text{m}$, as determined by the razor blade technique.^{90,91} We present a detailed step-by-step procedure to acquire and analyze Raman spectra throughout the fabrication of wafer scale SLG-based devices. This ensures quality control as well as reproducibility. The complete set of data we provide enables independent assessment of our results. [Tables 1](#) and [2](#) present a summary of the Raman fitting parameters and corresponding defect density, Fermi level (E_F), and strain.

Table 1. Raman Fit Parameters from [Figure 2d–g](#) and Corresponding Defect Density, E_F , and Strain

	SLG on SiO_2	SLG after Si_3N_4 deposition with hBN encapsulation	SLG after Si_3N_4 deposition without hBN encapsulation
Pos(G) (cm^{-1})	1585.5 ± 0.7	1590.3 ± 1.5	1590 ± 1.6
FWHM(G) (cm^{-1})	10.5 ± 1.0	11.8 ± 1.7	12.0 ± 1.9
Pos(2D) (cm^{-1})	2678 ± 1.2	2684.6 ± 1.8	2679.3 ± 1.8
FWHM(2D) (cm^{-1})	26.9 ± 0.8	32.5 ± 1.5	33.8 ± 2
$I(2D)/I(G)$	2.6 ± 0.3	2.3 ± 0.3	1.8 ± 0.2
$A(2D)/A(G)$	6.8 ± 0.6	6.5 ± 0.7	5.1 ± 0.5
$I(D)/I(G)$	<0.02	<0.05	0.48 ± 0.06
defect density (10^{11}cm^{-2})	<0.05	<0.10	1.98 ± 0.3
E_F (meV)	190 ± 30	220 ± 40	300 ± 40
uniaxial strain (%)	-0.08 ± 0.08	0.06 ± 0.12	-0.14 ± 0.12
(biaxial strain) (%)	(-0.03 ± 0.03)	(0.02 ± 0.04)	(-0.06 ± 0.05)

[Figure 2b](#) shows representative spectra of SLG on 285 nm SiO_2/Si , before (black) and after Si_3N_4 deposition, with (orange) and without (dark cyan) capping of SLG with 1L-hBN (see sketch in [Figure 2a](#)). The Raman signature of 1L-hBN is weak indicating the low quality of the commercial 1L-hBN.⁹² The transferred SLG spectrum has a 2D peak with a

Table 2. Raman Fit Parameters from Figure 3b–e and Corresponding Defect Density, E_F , and Strain

	SLG on SiO ₂	SLG after hBN encapsulation	SLG after Si ₃ N ₄ deposition	SLG on Si ₃ N ₄
Pos(G) (cm ⁻¹)	1583.1 ± 0.5	1584 ± 0.9	1593.8 ± 1.4	1582.3 ± 0.7
FWHM(G) (cm ⁻¹)	11 ± 1.1	12.2 ± 1.5	8.8 ± 1.9	14 ± 1.2
Pos(2D) (cm ⁻¹)	2675.2 ± 0.6	2678.5 ± 1.7	2687.1 ± 2.6	2674.1 ± 0.9
FWHM(2D) (cm ⁻¹)	23 ± 0.8	25.9 ± 1.3	32.7 ± 2.6	23.4 ± 1
I(2D)/I(G)	4.3 ± 0.4	3.9 ± 0.4	1.8 ± 0.3	4.6 ± 0.5
A(2D)/A(G)	8.9 ± 0.7	8.4 ± 0.8	6.8 ± 1.1	7.7 ± 0.7
I(D)/I(G)	<0.02	<0.02	0.11 ± 0.10	<0.05
defect density (10 ¹¹ cm ⁻²)	<0.05	<0.05	0.40 ± 0.4	<0.10
E_F (meV)	<100	<100	250 ± 50	<100
uniaxial strain (%)	0.07 ± 0.02	0.11 ± 0.03	0.13 ± 0.13	0.03 ± 0.04
(biaxial strain) (%)	(0.03 ± 0.01)	(0.04 ± 0.01)	(0.05 ± 0.05)	(0.01 ± 0.01)

single Lorentzian shape and with a full width at half-maximum FWHM (2D) \sim 26.7 cm⁻¹, a signature of SLG.⁹³ The G peak position, Pos(G), is \sim 1583.7 cm⁻¹, with FWHM(G) \sim 12.4 cm⁻¹. The 2D peak position, Pos(2D) is \sim 2676 cm⁻¹, while the 2D to G peak intensity and area ratios, I(2D)/I(G) and A(2D)/A(G), are \sim 3.1 and \sim 6.8, respectively. No D peak is observed, indicating negligible defects concentration.^{94,95} After Si₃N₄ deposition, the Raman spectrum of exposed SLG (*i.e.*, without 1L-hBN capping) has Pos(G) \sim 1590 cm⁻¹, FWHM(G) \sim 12 cm⁻¹, Pos(2D) \sim 2679 cm⁻¹, FWHM(2D) \sim 33.8 cm⁻¹, I(2D)/I(G) \sim 1.8, A(2D)/A(G) \sim 5.1, and I(D)/I(G) \sim 0.5. The latter indicates the creation of Raman active defects, which also act as scattering centers for the charge carriers^{96,97} (1 order of magnitude μ decrease was reported in ref 96 when going from I(D)/I(G) \sim 0.01 to \sim 0.5). Carrier scattering limits the performance of SLG EAMs, in terms of modulation efficiency (slope of the transmission variation as a function of applied voltage¹⁷) and maximum extinction ratio (ER)¹⁷ (*i.e.*, the ratio between maximum and minimum of light transmission¹⁷). The effect of defects on FWHM(G),⁹⁵ which remains almost unchanged after Si₃N₄ deposition, is likely compensated by the increased doping.⁹⁸ The Raman data indicate that E_F of SLG after transfer is \sim 170 meV (hole doping).^{99,100} E_F in the exposed SLG increases to \sim 290 meV.^{99,100}

SLG capping with 1L-hBN is used to protect SLG during PECVD (at 350 °C) of Si₃N₄. The SLG spectra with hBN capping after Si₃N₄ deposition have Pos(G) \sim 1590 cm⁻¹, FWHM(G) \sim 11.8 cm⁻¹, Pos(2D) \sim 2684 cm⁻¹, FWHM(2D) \sim 32.5 cm⁻¹, I(2D)/I(G) \sim 2.3, A(2D)/A(G) \sim 6.5. Figure 2c is a statistical comparison of I(D)/I(G) in 800 spectra from 2 SLG SCs with Si₃N₄ on top (400 spectra each), one protected by 1L-hBN (orange), the other exposed to PECVD (dark cyan). Ninety-eight percent of the spectra on hBN-encapsulated SLG have I(D)/I(G) < 0.1. One hundred percent of the nonencapsulated SLG have I(D)/I(G) > 0.1, with an average I(D)/I(G) \sim 0.48, corresponding to a defect concentration \sim 1.98 \times 10¹¹ cm⁻² (taking into account the finite doping \sim 300 meV).^{95,101} Hence, capping with 1L-hBN limits the creation of Raman active defects, therefore contributing to preserve μ .^{96,97} SLG SCs exposed to Si₃N₄ deposition present cracked areas with an average crack size \sim 10 μ m, as for the optical microscopy image in Figure 2c (right inset).

Raman mapping is performed at 1 μ m steps, over an area \sim 20 μ m \times 20 μ m on SLG transferred onto SiO₂/Si, and after Si₃N₄ deposition, with and without 1L-hBN. Figure 2d–g plots Raman data extracted from the maps: Pos(2D), FWHM(2D),

FWHM(G), A(2D)/A(G), as a function of Pos(G). Pos(G) depends on both doping^{99,100} and strain.¹⁰² The average Raman parameters from Figure 2d–g are in Table 1, together with the corresponding estimates of defect density, E_F , and strain.

The Raman data indicate E_F after transfer \sim 190 meV (hole doping).^{99,100} HBN capping, in addition to limiting the generation of Raman active defects, keeps E_F close to that of transferred SLG (\sim 220 meV). E_F in exposed SLG increases to \sim 300 meV.^{99,100}

The Grüneisen parameters¹⁰² rule the change of Pos(2D) and Pos(G) in response to strain. The G and 2D peaks do (do not) split for increasing uniaxial (biaxial) strain.⁹⁴ At low (\leq 0.5%) strain the splitting cannot be resolved.^{102,103} Figure 3d plots the correlation between Pos(2D) and Pos(G). Linear fits in Figure 3d give a slope Δ Pos(2D)/ Δ Pos(G) \sim 1.37, 0.85, 1.1 for SLG after transfer, after Si₃N₄ with hBN, and without hBN, respectively. The slopes indicate that both doping and strain variations are present. We cannot exclude the presence (or coexistence) of biaxial strain. For uniaxial (biaxial) strain, Pos(G) shifts by Δ Pos(G)/ Δ ϵ \sim 23(60) cm⁻¹/%.^{102–104} For intrinsic SLG (E_F < 100 meV), the unstrained, undoped Pos(G) is \sim 1581.5 cm⁻¹.^{93,105} Taking into account the shift in Pos(G) due to finite doping (E_F \sim 190, 220, 300 meV for the three cases), we estimate a mean uniaxial(biaxial) strain ϵ \sim -0.08% (\sim -0.03%) for the transferred SLG, and \sim 0.06% (\sim 0.02%) and \sim -0.14% (\sim -0.06%) for the hBN-capped and exposed SLG after Si₃N₄ deposition, respectively.

After 1L-hBN-capping and PECVD deposition of Si₃N₄, DSLGs are completed by transferring top-layer SLG arrays onto Si₃N₄ by semidry transfer. The use of identical deterministically grown SC matrices ensures that bottom and top SLG overlap over the entire wafer area, enabling wafer-scale fabrication.

The assembly of DSLG is monitored by Raman spectroscopy. We collect 8909 spectra on 48 crystals (24 bottom-layer and 24 top-layer) over four portions of a 150 mm wafer (p-doped Si with 285 nm SiO₂). Figure 3a plots representative spectra taken after the main assembly steps: (1) transfer of bottom SLG arrays on SiO₂/Si (black), (2) transfer of 1L-hBN (red), (3) deposition of Si₃N₄ (orange), and (4) transfer of top SLG on Si₃N₄ (purple). The SLG spectra after transfer on SiO₂ (bottom-layer, black) and on Si₃N₄ (top-layer, purple) have a 2D peak with a single Lorentzian shape and FWHM(2D) \sim 22.2 and 23.1 cm⁻¹, respectively. Pos(G) is \sim 1583.1 cm⁻¹ for SLG on SiO₂ and \sim 1582.1 cm⁻¹ for SLG on Si₃N₄, with FWHM(G) \sim 10.6 and 14.5 cm⁻¹, respectively. Pos(2D) is

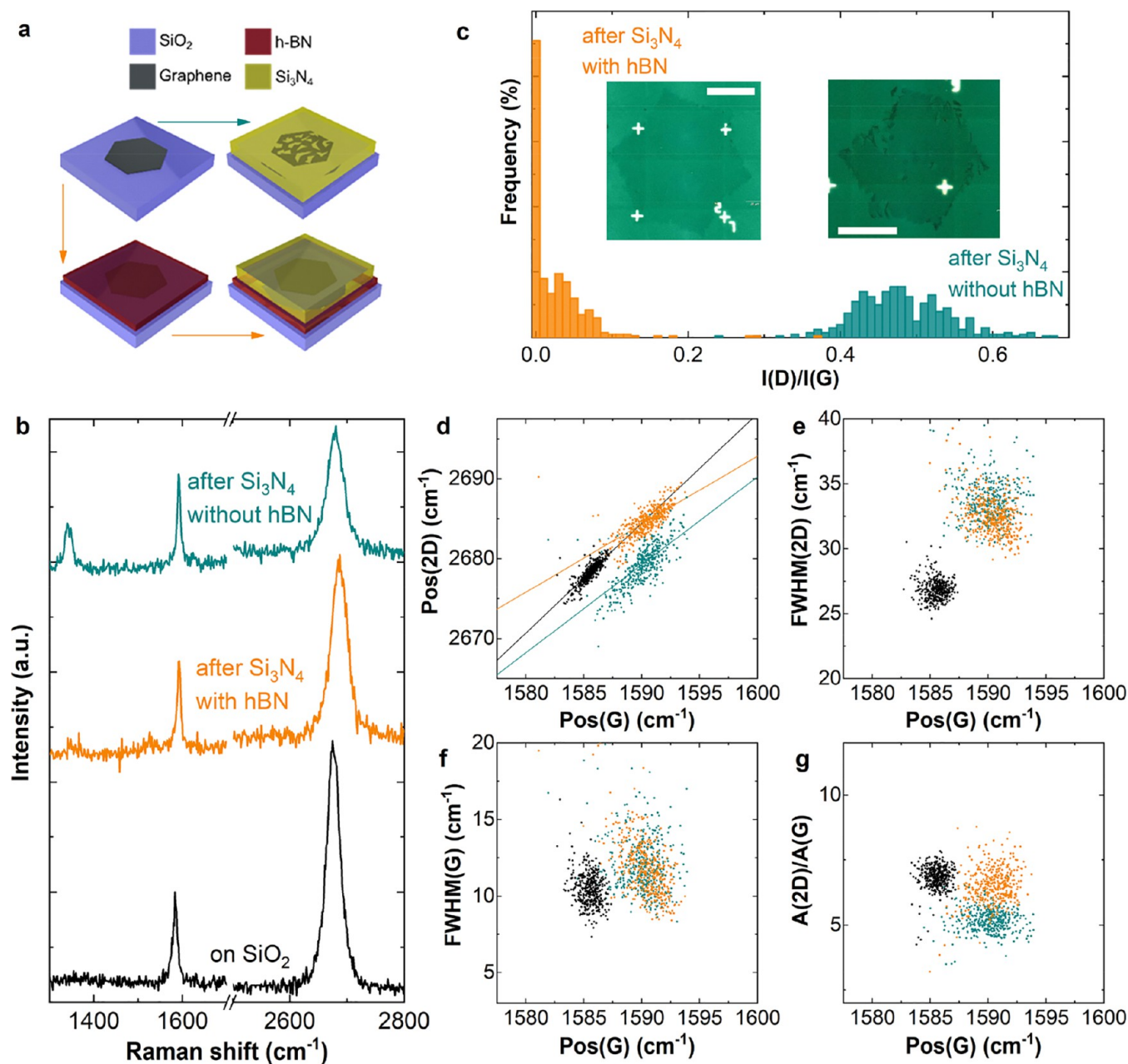


Figure 2. (a) Schematic representation of PECVD deposition of Si₃N₄ on SLG without (top, dark cyan arrow) and with (bottom, orange arrows) intermediate 1L-hBN. (b) Typical Raman spectra on SLG SCs after transfer (black) after Si₃N₄ PECVD, with (orange) and without (dark cyan) 1L-hBN. The same colors are used in the correlation plots d–g. (c) Distribution of $I(D)/I(G)$ from 800 spectra acquired on two SLG SCs, one protected (orange bars), the other exposed (dark cyan bars). Inset: optical micrographs of the two SCs, showing cracked areas in the exposed one. Scale bars 50 μm . (d) $\text{Pos}(2D)$ as a function of $\text{Pos}(G)$. Solid lines are linear fits of the data. (e) $\text{FWHM}(2D)$ as a function of $\text{Pos}(G)$. (f) $\text{FWHM}(G)$ as a function of $\text{Pos}(G)$. (g) $A(2D)/A(G)$ as a function of $\text{Pos}(G)$.

~ 2675.3 and ~ 2673.9 cm^{-1} , while $I(2D)/I(G)$ and $A(2D)/A(G)$, are ~ 4.5 (on SiO₂), ~ 5 (on Si₃N₄), ~ 9.5 (on SiO₂), and ~ 8 (on Si₃N₄). No D peak is observed, indicating negligible defect concentration.^{94,95} The difference in $\text{FWHM}(G)$ indicates reduced doping for the top-layer SLG on Si₃N₄.^{99,106} The bottom-layer SLG spectra with hBN capping before (red) and after (orange) Si₃N₄ deposition have both a 2D peak with a single Lorentzian shape and $\text{FWHM}(2D) \sim 24.6$ and 32.2 cm^{-1} . $\text{Pos}(G)$ is ~ 1583.9 and ~ 1593.6 cm^{-1} for hBN-capped SLG before and after Si₃N₄ deposition, with $\text{FWHM}(G) \sim 11.4$ and 8.6 cm^{-1} , $\text{Pos}(2D) \sim 2678.7$ and 2686.8 cm^{-1} . $I(2D)/I(G)$ and $A(2D)/A(G)$ are ~ 4.1 and

~ 8.9 before and ~ 1.9 and ~ 7.2 after the Si₃N₄ deposition. The shift of $\text{Pos}(G)$ and decrease of $\text{FWHM}(G)$, together with decrease of $I(2D)/I(G)$ and $A(2D)/A(G)$, indicate an increase in defect density, E_F , upon Si₃N₄ deposition.^{99,100} In addition, a considerable (2500 cps at 1 mW power excitation) photoluminescence background is observed after Si₃N₄ deposition, which we attribute to the introduction of defects in 1L-hBN.¹⁰⁷ The broad band is peaked at ~ 600 nm (inset, Figure 3a) similar to defect related broad emission in 1L-hBN.¹⁰⁷ Raman mapping is then performed on the SLG arrays at 10 μm steps. Figure 3b–e plots $\text{Pos}(2D)$, $\text{FWHM}(2D)$, $\text{FWHM}(G)$, and $A(2D)/A(G)$ as a function of $\text{Pos}(G)$. Local variations in

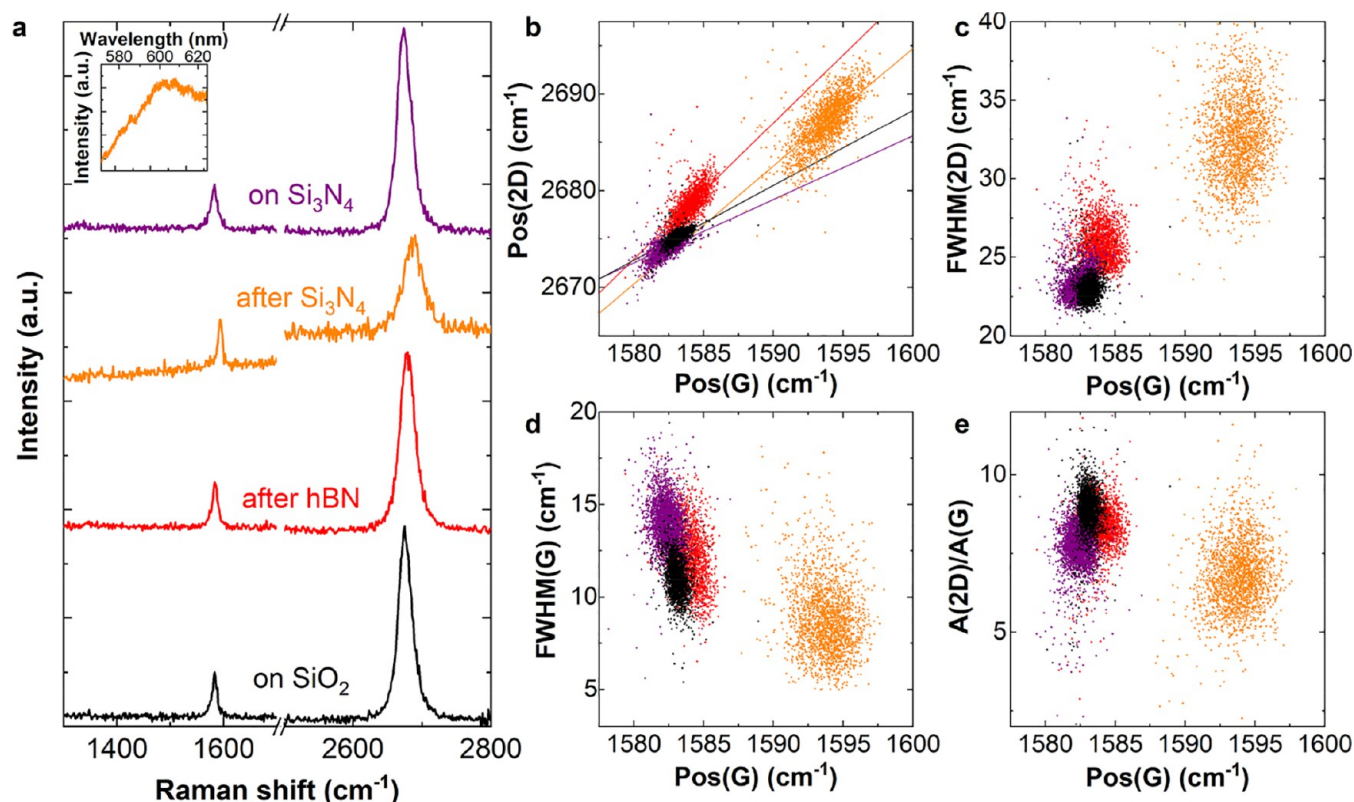


Figure 3. (a) Representative spectra of SLG SCs for the different fabrication steps. Inset: photoluminescence of 1L-hBN after Si_3N_4 deposition. (b–e) $\text{Pos}(2\text{D})$, $\text{FWHM}(2\text{D})$, $\text{FWHM}(\text{G})$, $A(2\text{D})/A(\text{G})$ as a function of $\text{Pos}(\text{G})$. The color code is the same as in panel a.

strain⁹⁸ and doping^{98,99} produce a spread in $\text{Pos}(\text{G})$. The average Raman data of Figure 3b–e are presented in Table 2.

The bottom-layer SLG, transferred and after hBN-capping, and top-layer SLG, are within the intrinsic SLG range in terms of doping ($E_{\text{F}} < 100$ meV).^{99,100} After Si_3N_4 deposition, the bottom-layer E_{F} increases to ~ 250 meV.^{99,100} The linear fit to $\text{Pos}(2\text{D})$ as a function of $\text{Pos}(\text{G})$ in Figure 3b gives $\Delta\text{Pos}(2\text{D})/\Delta\text{Pos}(\text{G}) \sim 0.78, 0.66, 1.41, 1.22$ for bottom-layer SLG transferred on SiO_2 , top-layer on Si_3N_4 , bottom-layer after hBN capping, and bottom-layer after Si_3N_4 deposition, respectively. This indicates the coexistence of strain and doping, modulated during the assembly steps. The presence (or coexistence) of biaxial strain cannot be ruled out. Considering the Grüneisen parameters^{102–104} and the unstrained, undoped $\text{Pos}(\text{G})$ ^{93,105} for intrinsic SLG as above, we estimate a mean uniaxial(biaxial) strain $\epsilon \sim 0.07\%$ ($\sim 0.03\%$) and 0.03% ($\sim 0.01\%$), for SLG after transferring on SiO_2 (bottom-layer) and on Si_3N_4 (top-layer), respectively. The bottom SLG after hBN capping has $\epsilon \sim 0.1\%$ ($\sim 0.04\%$) while, after Si_3N_4 deposition, considering doping,⁹⁸ $\epsilon \sim 0.13\%$ ($\sim 0.05\%$).

To monitor the uniformity of the Raman response throughout the fabrication of the DSLGs, we map 48 SLG SCs, 24 bottom-layer (b1–4 arrays), and 24 top-layer (t1–4 arrays), on four different portions of a 150 mm wafer. Figure 4 plots false-color maps of $I(\text{D})/I(\text{G})$, $\text{FWHM}(2\text{D})$, $\text{FWHM}(\text{G})$, $A(2\text{D})/A(\text{G})$ for the four assembly stages. Each map is taken with $10 \mu\text{m}$ steps. At a given stage, the Raman data do not show significant variations between SLG belonging to the same portion of the wafer. The same applies to SLG from different parts. This implies that the spread in points in Figure 3b–e is representative of the variation of the Raman

peaks within individual SLG SCs while, over the scale of the entire wafer, SLG SCs have uniform properties. Small ($10\text{--}20 \mu\text{m}$ wide) bilayer graphene (BLG) regions form at nucleation seeds during CVD (on 38/48 of the analyzed crystals, see broad 2D peak central pixels in Figure 4b⁹³).

$I(\text{D})/I(\text{G})$, Figure 4a, is negligible throughout the fabrication, except for b1–4 after Si_3N_4 deposition, where it is within 0.1 (0.25) for 59% (90%) of the crystals (see also the average values in Table 2). $\text{FWHM}(2\text{D})$, Figure 4b, progressively increases upon fabrication on b1–4, while it is comparable for b1–4 and t1–4 after transfer on SiO_2 and Si_3N_4 . $\text{FWHM}(\text{G})$ and $A(2\text{D})/A(\text{G})$, Figure 4c,d, are comparable for all SLG SCs, except for b1–4 after Si_3N_4 deposition, where they decrease due to $E_{\text{F}} > 100$ meV.

Thus, our wafer-scale Raman characterization reveals that the top-SLG in the DSLG is comparable to micromechanically exfoliated flakes in terms of doping,⁹⁹ strain,¹⁰⁸ and strain fluctuations.^{109,110} The transfer of hBN has marginal effect on the properties of the bottom-SLG. However, it plays a key role in preserving the structural integrity of the crystals, and avoiding the formation of Raman-active defects during Si_3N_4 deposition, thus preventing μ degradation. The Raman analysis shows an increase in doping, strain and strain fluctuations in the bottom SLG after the PECVD process. However, the PECVD process results in a homogeneous dielectric layer, crucial for reproducible operation of DSLG modulators.³⁴

We then investigate the electrical transport properties of the transferred SLG-SCs using back-gated multiterminal devices at RT and exposed to air. This allows us to monitor two key performance parameters for SLG integration in a photonic circuit: contact resistance (R_{c}) and μ .

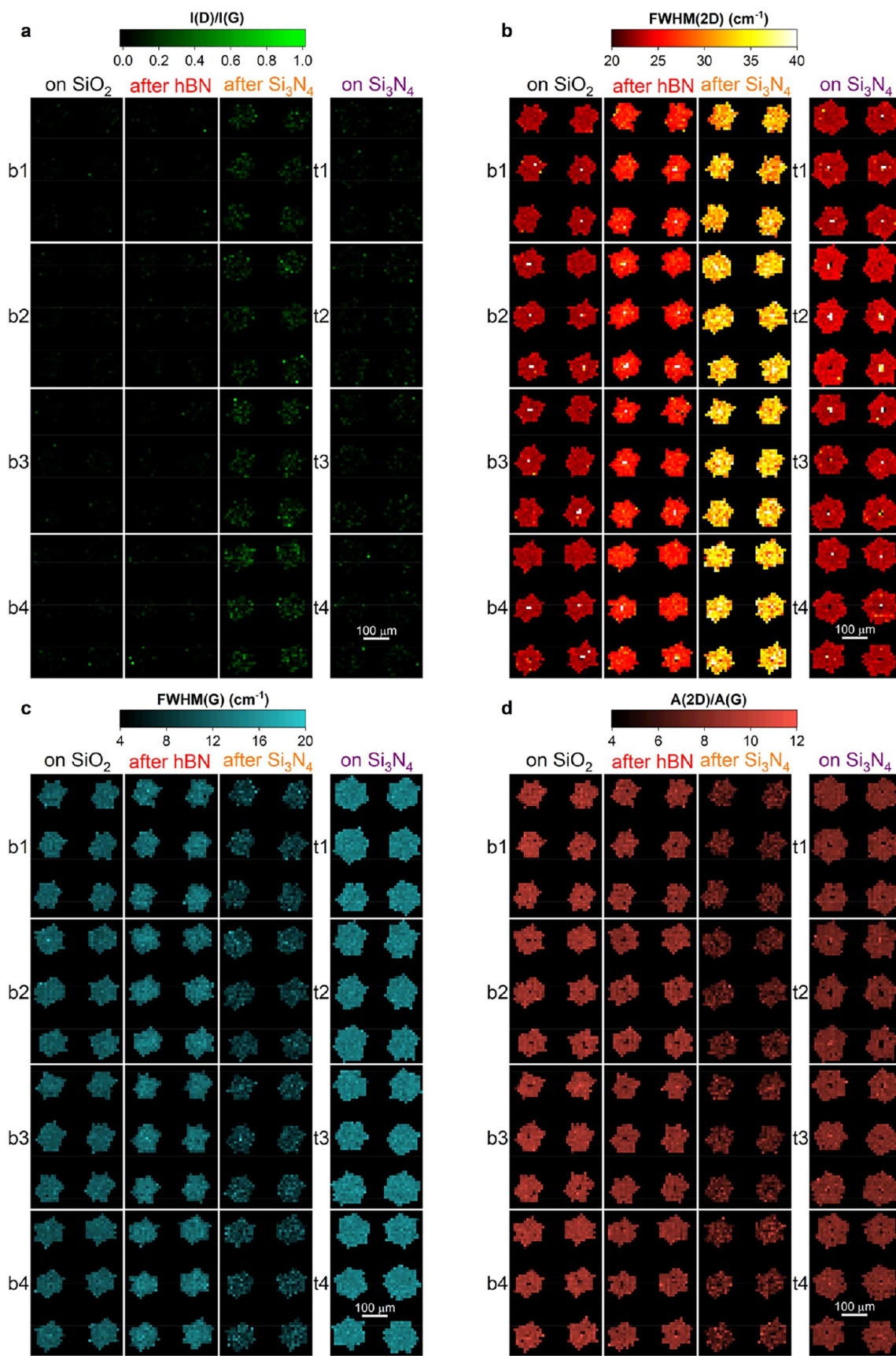


Figure 4. Wafer-scale Raman mapping at each fabrication step over different quadrants of the wafer. (a–d) Maps of I(D)/I(G), FWHM(2D), FWHM(G), A(2D)/A(G). Raman mapping is performed at each assembly stage over bottom (b1–4) and top SLG arrays (t1–4).

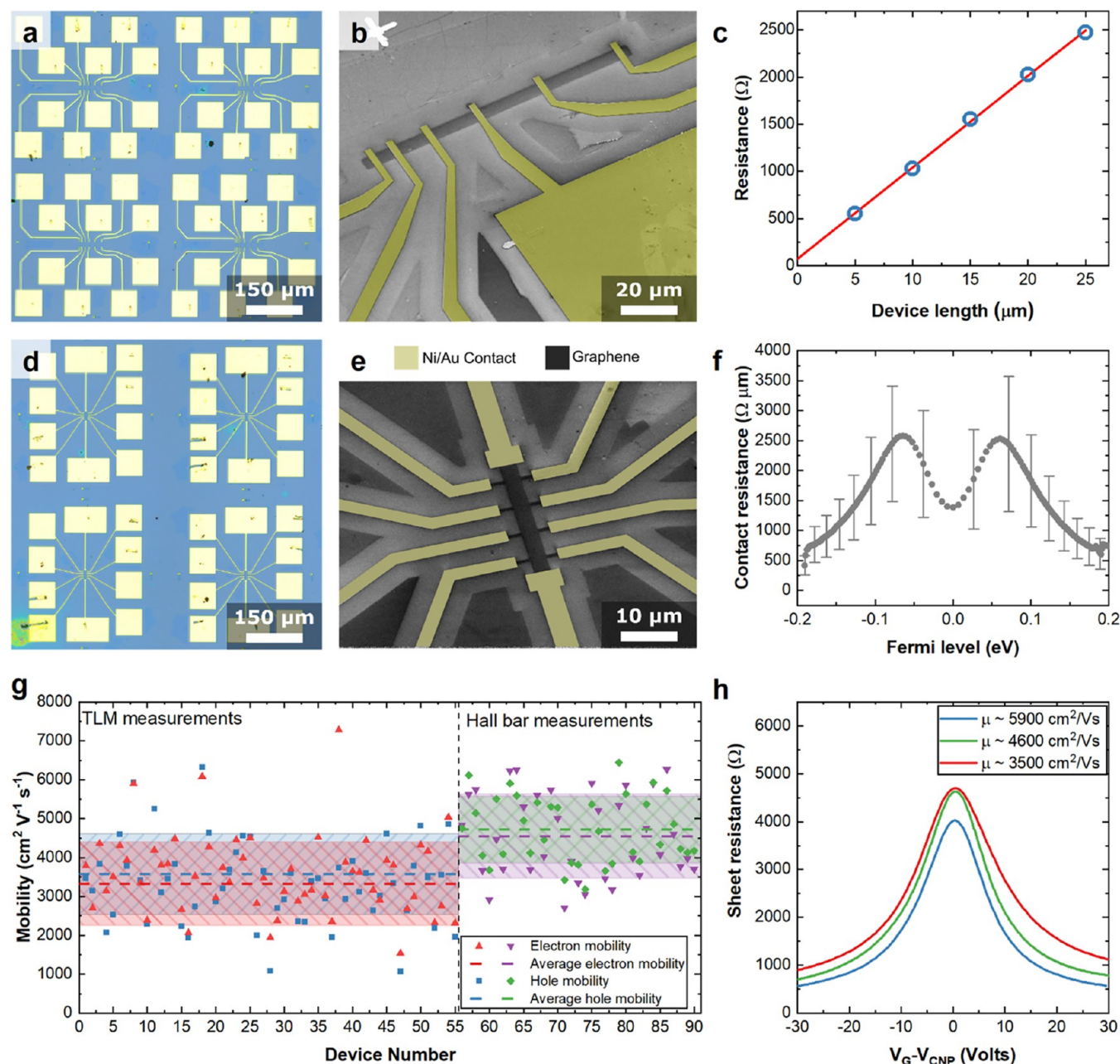


Figure 5. Wafer-scale electrical characterization. (a) Optical micrograph of TLM structures. (b) SEM image of representative TLM structure. (c) Estimation of R_C via linear fit of TLM measurements. (d) Optical micrograph of Hall bars. (e) SEM image of representative Hall bar. (f) R_C as a function of E_F . (g) Statistics of e and h mobility from TLM and Hall measurements. Dashed lines represent the average μ . Shaded areas indicate the standard deviation. (h) Representative field effect curves for 3 Hall bars with $\mu \sim 3500$, ~ 4600 , ~ 5900 $\text{cm}^2 \text{V}^{-1} \text{s}^{-1}$.

To quantify R_C , we use transfer-length method (TLM)¹¹¹ devices, as in Figure 5a,b, defined by EBL, reactive-ion etching and thermal evaporation of metallic contacts. Ni/Au 7/60 nm top contacts evaporated $<10^{-5}$ mbar provide the highest performing configuration in terms of yield ($>80\%$ of working devices) and R_C when compared to Cr, Ti, and Ni and to other contact geometries, such as one-dimensional side contacts.¹¹²

By measuring the two-terminal resistance over different channel lengths (l) we extrapolate the residual resistance at $l = 0$, which corresponds to $2 \times R_C$,¹¹¹ Figure 5c. This procedure can be repeated for different E_F , set by the back-gate voltage (V_G), to obtain R_C as a function of E_F , as for Figure 5f, showing the statistical average over 56 devices and error bars as standard deviations. R_C remains $<2500 \text{ } \Omega \mu\text{m}$ in the neutrality

region and is $\sim 500 \text{ } \Omega \mu\text{m}$ for $E_F > 0.2$ eV, required in the operation of modulators at telecom wavelengths.² The SLG E_F must be set at energies larger than half of the photon energy in order to work at the edge of Pauli blocking.^{42,43,113} At 1550 nm the photon energy is 0.8 eV, so that E_F must be set slightly above 0.4 eV.³⁴ These R_C are comparable to those previously reported for ultrahigh $\mu > 10^5 \text{ cm}^2 \text{V}^{-1} \text{s}^{-1}$ devices.¹¹² We get μ from 56 TLM structures as well as 36 Hall bars, in Figure 5d,f. The SLG resistivity, ρ , for the TLM devices is obtained from a linear fit of TLM channels (Figure 5c) as a function of V_G . The Hall bar ρ is derived from four-terminal measurements and fitted as for ref 114. In Figure 5g, dashed lines indicate the average μ for both e and h , whereas the shaded areas represent the standard deviation. The average μ from Hall bars (~ 4750

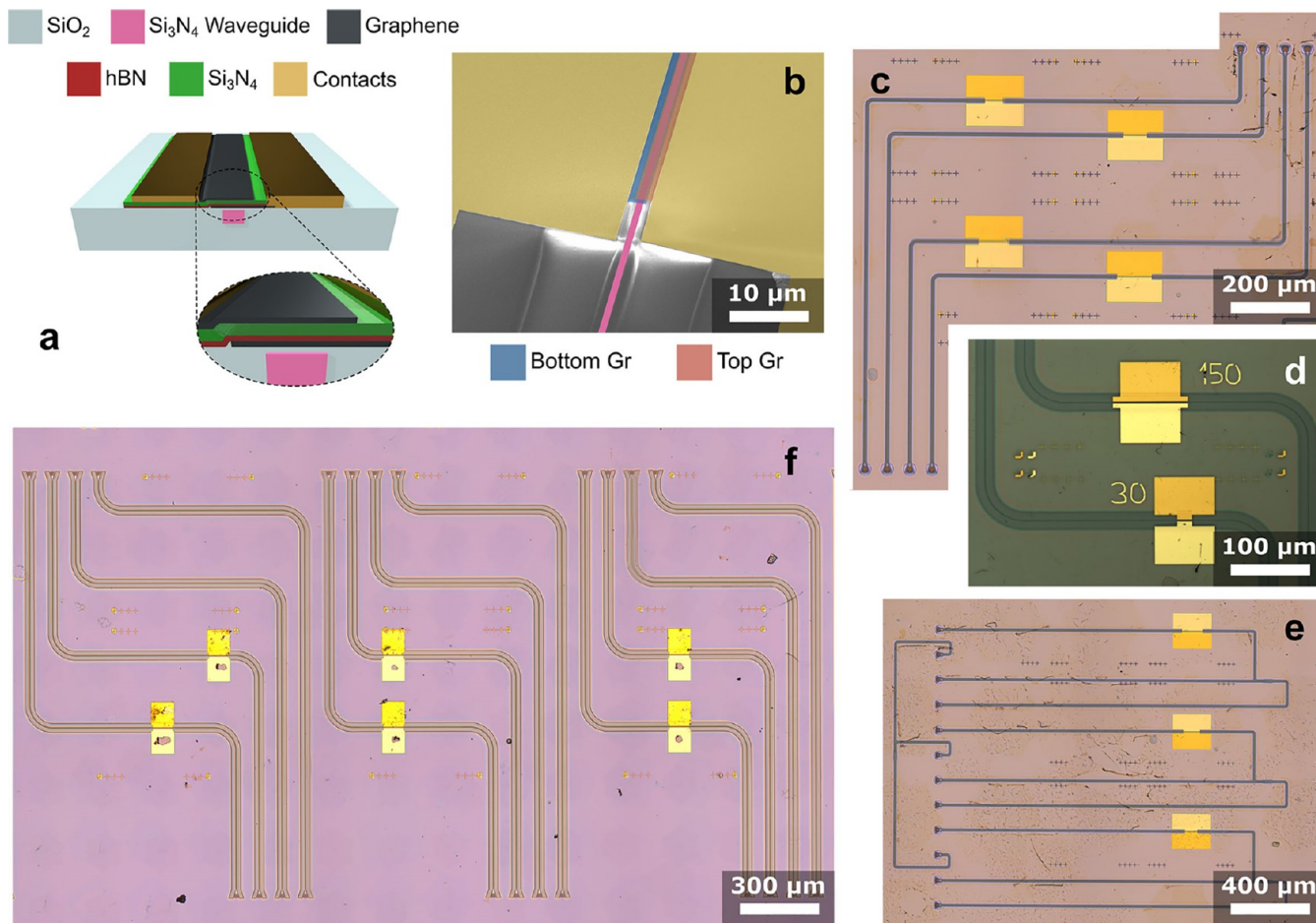


Figure 6. (a) Cross-section of DSLG EAMs. The Si_3N_4 WG core is 1500 nm wide and 260 nm thick, the buried oxide is $15\ \mu\text{m}$, and the distance of the metal electrodes from the WG edge is 700 nm. (b) SEM image of DSLG EAM showing the overlap of the two SLG (blue and red) above the photonics WG (pink). (c–f) Optical micrographs of four chips with DSLG EAMs.

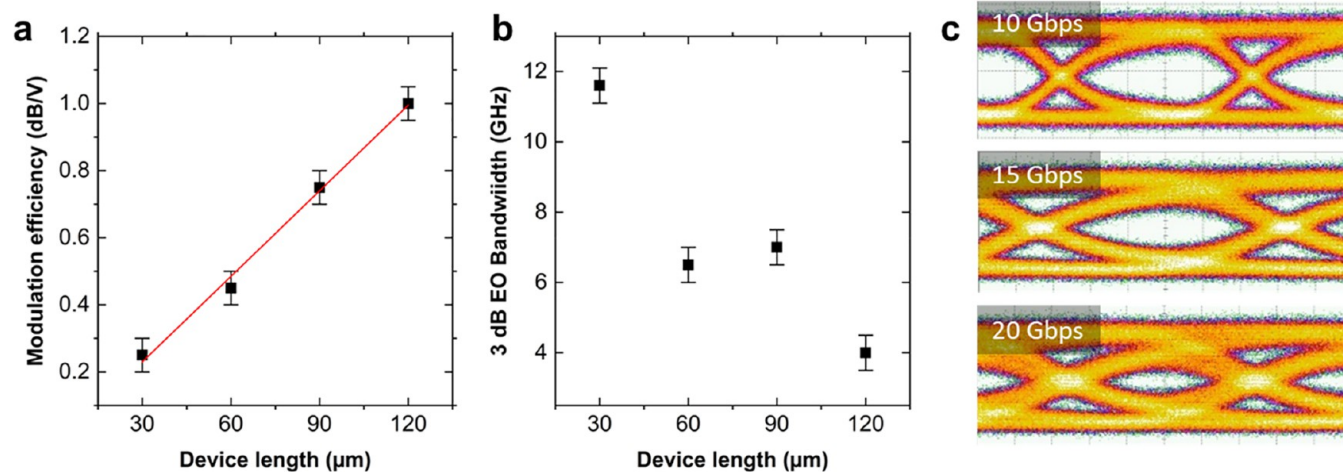


Figure 7. DSLG EAM characterization. (a) Modulation efficiency as a function of device length. (b) 3 dB EO BW as a function of devices length (c) Eye diagrams at 10, 15, and 20 Gbps.

$\text{cm}^2\ \text{V}^{-1}\ \text{s}^{-1}$ for h and $\sim 4600\ \text{cm}^2\ \text{V}^{-1}\ \text{s}^{-1}$ for e) is higher than TLM (~ 3600 and $\sim 3350\ \text{cm}^2\ \text{V}^{-1}\ \text{s}^{-1}$, respectively). This could be caused by two factors. (1) For each TLM, ρ is estimated from an average of 5 channels, with a total length of $75\ \mu\text{m}$, whereas the channel length in a Hall bar is $8\ \mu\text{m}$, comparable to that used in typical SLG transport measurements.¹¹⁴ (2) Parasitic doping by the contacts has an effect in

two-terminal TLM measurements,^{115,116} not present in four-terminal Hall bar measurements.¹¹⁷ Figure 5h plots 3 representative traces of ρ as a function of V_G from Hall bars with high ($\sim 5900\ \text{cm}^2\ \text{V}^{-1}\ \text{s}^{-1}$), low ($\sim 3500\ \text{cm}^2\ \text{V}^{-1}\ \text{s}^{-1}$), and average ($\sim 4700\ \text{cm}^2\ \text{V}^{-1}\ \text{s}^{-1}$) μ .

EAMs are based on the modulation of the surface optical conductivity at optical frequencies induced by electric field

effect.^{41,118} SLG absorption is changed by moving E_F above the Pauli blocking condition.^{42,43,113} This can be done by applying gating in a capacitor-like structure, with SLG used as one or both capacitor plates.² In our DSLG geometry, a reciprocal self-gating is obtained with V_G , resulting in modulation of the surface carrier density, *i.e.*, electro-absorption.³⁴ The main advantages of this approach are the larger electro-absorption effect, due to the presence of two SLG, approximately twice that of SLG,³⁴ and the possibility to use undoped WGs, enabling integration onto any already existing platform, such as SOI for SiPh or Si_3N_4 on Si.³⁴

Here we use a 150 nm Si_3N_4 photonic platform, with 260 nm Si_3N_4 on a 15 μm buried SiO_2 . The 1500 nm wide WG is designed to support a transverse-electric field (quasi-TE) mode at 1550 nm.¹⁷ The top cladding is thinned to ~ 40 nm to maximize the evanescent coupling of the optical mode with the DSLG stack. The core of the modulators is the DSLG capacitor, comprising a SLG/hBN/ Si_3N_4 /SLG stack. The cross-section and a SEM image of a representative device is in Figure 6a,b (see the Methods for details). We prepare 30 SLG/hBN/ Si_3N_4 /SLG stacks on 30 WGs to fabricate 30 EAMs with different lengths (Figure 6c–f). This allows us to benchmark the reproducibility of the fabrication process at wafer scale through optoelectronic characterization of the devices.

We test key performance parameters: static (DC-biased) and dynamic (DC-biased + RF) modulation depth, electro-optical (EO) BW, and eye diagram opening. We characterize the EAMs in static and dynamic (*i.e.*, driven by a time varying electrical signal) mode and collect the data to perform a statistical study of performance, Figure 7. We first consider the transmission as a function of V_G . Modulation is obtained by tuning E_F of both SLG layers from complete optical absorption ($E_F < 0.4$ eV at 1550 nm) toward transparency ($E_F > 0.4$ eV).³⁴ The static characterization on wafer scale shows modulation efficiency $\sim 0.25, 0.45, 0.75, 1$ dB V^{-1} for $\sim 30, 60, 90, 120$ μm EAMs, respectively, Figure 7a. We then characterize the EO BW, *i.e.*, the BW of the conversion efficiency, defined as the ratio between the output and the input power,¹⁷ from the electrical signal driving the modulator and the optical modulated signal at the output of the modulator.¹⁷ This parameter determines the maximum operating speed and is typically affected by R_C .¹¹⁹ The EAM BW is mainly limited by its RC time constant,¹¹⁹ *i.e.*, the series resistance (R) of the device multiplied by the DSLG capacitance, C , given by the series of gate dielectric capacitance and quantum capacitance of the two SLGs,¹²⁰ with $R = R_C + R_S$ of the SLG section between DSLG capacitor and metal contacts. As C is proportional to the device length, while R is inversely proportional to it, we would expect a length-independent 3 dB electro-optical BW. However, Figure 7b shows that the BW changes with length, with longer devices having lower BW. We obtain $\sim 11.5, 6.5, 7.4$ GHz for 30, 60, 120 μm , respectively. The reason is that a further contribution to R comes from the output 50 Ω impedance of the vector network analyzer (VNA) used to perform the measurements (see the Methods). This is the main limiting resistive contribution because of our low $R_C \sim 500$ Ω μm at $E_F > 0.2$ eV.

We then test the DSLG EAMs using a non-return-to-zero (NRZ) electrical driving signal,⁵⁸ *i.e.*, a digital two-level sequence, generated with a pattern generator (PG) (Anritzu MP1800A). This instrument allows us to obtain pseudorandom binary sequences (PRBS), *i.e.*, deterministic binary sequences of bits with statistical behavior similar to a pure

random sequence,²⁷ with adjustable lengths (up to $2^{31}-1$ bits). The signal is applied to the DSLG EAMs electrodes through a RF cable and a bias-tee. This generates a modulated optical signal, detected by a high-frequency (70 GHz) photodetector (Finisar XPDV3120) connected to a sampling digital oscilloscope (Infinium DCA 83484A, BW ~ 50 GHz). By doing so, we can visualize on the oscilloscope the resulting eye diagram,¹²¹ Figure 7c. This gives the frequency dependent ER and 3 dB EO BW as a function of device length, and 10/15/20 Gbps data-rate.¹²¹ The eye diagram measurement of the data stream along with ER and 3 dB EO BW demonstrate EAM at 20 Gbps on wafer scale. Our wafer-scale fabrication approach may also be used on different photonic platforms, *e.g.*, SOI. The smaller WG cross section, 480 nm \times 220 nm, would reduce the modulator stack capacitance, thus improving EAM speed.

The change from Si_3N_4 to SOI, as reported in ref 47, increases the EO BW to at least 30 GHz, and the data rate to 50 Gbps in a 100 μm EAM. Improving the SLG quality, in terms of μ after Si_3N_4 encapsulation, can increase performance in terms of insertion loss per unit length. Assuming a maximum absorption ~ 0.1 and < 0.001 dB μm^{-1} in the transparency region for $\mu > 3000$ $\text{cm}^2 \text{V}^{-1} \text{s}^{-1}$ at 0.4 eV, the EAM length can be reduced to 50 μm , with a maximum ER = 5 dB and a halved capacitance. By reducing the RC constant, we expect to approximately double its BW with respect to the 100 μm device, thus achieving ~ 60 GHz. This optimization, combined with a SOI WG, could result in EAMs competitive with present microring based SOI modulators^{28,122} and SiGe EAMs.²⁹ The added value of SLG-based EAMs is the broad operation spectrum, from O (1300 nm) to L-band (> 1625 nm) and beyond, while SiGe modulators are restricted to the C band (1530–1565 nm),¹²³ and Si microring modulators are limited to resonant wavelengths.¹²⁴

CONCLUSIONS

We presented the full process flow (from growth, to transfer, integration on WGs, and photonic devices fabrication) for SLG-based photonics on wafer-scale. Our approach yields high-quality uniform SLG on wafer-scale, as indicated by statistical spectroscopic and electrical characterizations. We used wafer scale hBN encapsulation to minimize damage during dielectric deposition. We applied this to realize double SLG electro-absorption modulators on the passive Si_3N_4 platform. Our approach is easier and more reproducible, in terms of yield and uniformity, compared to the transfer of a continuous SLG film over the full wafer area, because it is based on individual crystal matrices. SLG single crystals have higher mobility than polycrystalline films, with high-quality top contacts, with a reproducible contact resistance ~ 500 Ω μm . Our approach can be used for other photonics building blocks, such as photodetectors and mixers, as well as for resonant structures, including microrings for modulation, switching and filtering, and nonresonant ones, like interferometers.

METHODS

SLG crystal matrices are grown on 25 μm Cu foils (Alfa Aesar no. 46365). Prior to SLG growth, each foil is electropolished in an electrolyte consisting of water, ethanol, phosphoric acid, isopropyl alcohol, and urea, as for ref 79. The Cu foil is patterned using UV lithography. Cu is spin-coated with a Shipley S1813 positive photoresist, baked at 110 $^\circ\text{C}$ for 1 min, and exposed to UV light using a Cr mask containing the required seeding pattern (UV dose

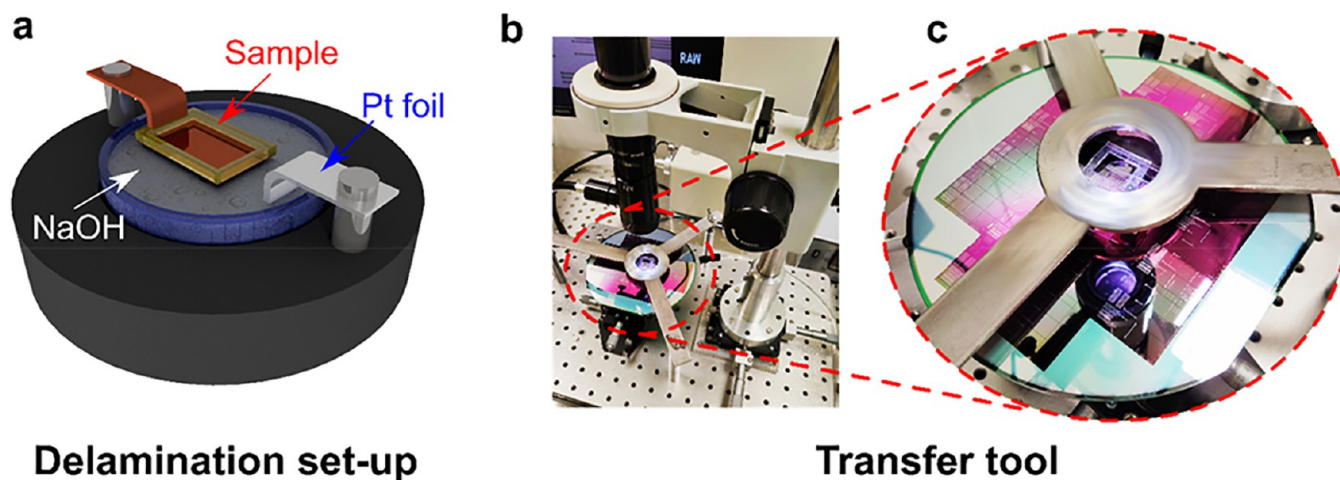


Figure 8. (a) Schematic electrochemical delamination setup. (b) Transfer tool holding the delaminated SLG sample and a 150 mm Si_3N_4 wafer patterned with the photonic WG circuits of Figure 6. (c) Close-up of SLG/PMMA membrane, with a PDMS frame aligned onto the target wafer.

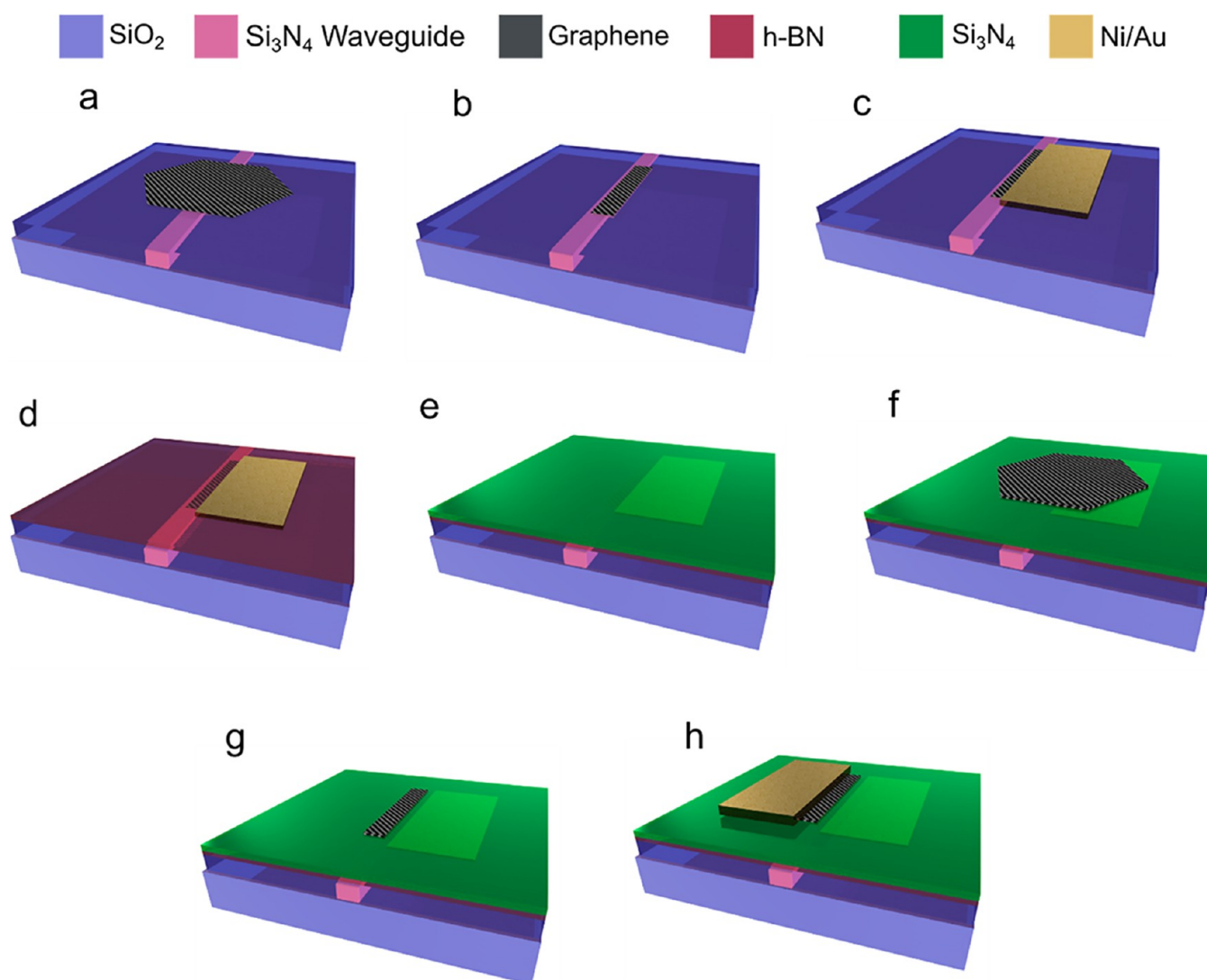


Figure 9. Process flow for DSLG EAM fabrication. (a) SC SLG transfer on WG. (b) SLG patterning using EBL and RIE. (c) Ni/Au contacts deposition using evaporation and lift-off. (d) 1L-hBN transfer on top. (e) Si_3N_4 deposition by PECVD. (f) Top layer SLG SC transfer. (g) Top SLG patterning. (h) Top contact deposition.

$\sim 200 \text{ mJ cm}^{-2}$). Twenty-five nanometer Cr is thermally evaporated (Sistec) at 1×10^{-5} mbar, followed by lift-off in acetone. The samples are then rinsed in isopropyl alcohol. Growth is performed in an Aixtron BM Pro cold-wall reactor at 25 mbar and $1060 \text{ }^\circ\text{C}$. The samples are kept under Ar flow during the T ramp-up, and are annealed for 10 min at the growth T. Growth is performed by flowing 0.5 sccm CH_4 , 50 sccm H_2 and 900 sccm Ar . Following the 20 min growth, heating is switched off and the sample is cooled to $<120 \text{ }^\circ\text{C}$ under Ar flow.

SLG on Cu is then coated with a support polymer (100 nm PMMA 950 K and $1.5 \text{ } \mu\text{m}$ PPC) and a PDMS frame is attached to the perimeter of the Cu foil. SLG electrochemical delamination is performed in 1 M NaOH . Cu/SLG is used as the anode, and $\sim 2.4 \text{ V}$ is applied with respect to a Pt counter electrode, Figure 8a. The voltage is adjusted to maintain a current $\sim 3 \text{ mA}$ to avoid excessive formation of H_2 bubbles, which may cause damage to SLG. The freestanding polymer/SLG membrane is then removed from the electrolyte, rinsed 3 times in DI water, then dried in air.

The lamination of SLG on the target wafer is performed in a transfer tool, shown in Figure 8b, with a close-up of the SLG/PMMA membrane with a PDMS frame aligned onto the target wafer in Figure 8c. The target wafer is placed on a micrometric stage with three-axis translational and azimuthal rotational movement, Figure 8b. Alignment of the WGs to the SLG SC matrix is performed exploiting the SLG contrast on the polymer membrane in transmission mode, Figure 1d. The optical system of the transfer tool consists of a $0.58\text{--}7\times$ microscope objective with coaxial illumination, and a DSLR camera with a $2\times$ adapter tube, giving a final magnification $\sim 1.16\text{--}14\times$.

Following alignment, the wafer is heated to $100 \text{ }^\circ\text{C}$ using the inbuilt stage heater with a proportional-integral-derivative (PID) controller, and the membrane is brought into contact with the wafer to laminate the SLG. Heating the wafer reduces the adhesion of PDMS, and the frame can be then detached from the wafer, Figure 7b. Depending on the geometry of the wafer, several cycles of the above procedure are performed to populate the wafer with SLG SCs. For a typical SLG SC matrix of $25 \times 40 \text{ mm}^2$, 16 cycles populate 90% of a 150 mm wafer. Finally, the wafer is placed in acetone to remove the support polymer, followed by a rinse in isopropyl alcohol.

The fabrication of the DSLG modulator stack is performed as follows. A matrix of SLG SCs is transferred on the target wafer and aligned to the Si_3N_4 WG, Figure 9a. The bottom layer SLG is spin-coated with PMMA 950 A4 (Microchem), patterned using EBL and etched using RIE, Figure 9b. Contacts to the bottom SLG are fabricated using EBL and thermal evaporation of 7 nm Ni and 60 nm Au , followed by lift-off in acetone, Figure 9c. A $2 \times 2.5 \text{ cm}^2$ polycrystalline 1L-hBN (Graphene Laboratories, Inc.) grown on Cu foil via CVD¹²⁵ is then electrochemically delaminated from Cu and transferred on the chips of the wafer via semidry transfer.⁷⁶ Si_3N_4 (17 nm) is deposited using PECVD at $350 \text{ }^\circ\text{C}$, Figure 9e. The top layer of the modulator is fabricated following the same protocol of transfer (Figure 9f), etching (Figure 9g), and contacting (Figure 9h).

AUTHOR INFORMATION

Corresponding Authors

Camilla Coletti – Center for Nanotechnology Innovation @ NEST - Istituto Italiano di Tecnologia, I-56127 Pisa, Italy; Graphene Labs, Istituto Italiano di Tecnologia, 16163 Genova, Italy; orcid.org/0000-0002-8134-7633; Email: camilla.coletti@iit.it

Marco Romagnoli – Photonic Networks and Technologies Lab, CNIT, 56124 Pisa, Italy; INPHOTEC, 56124 Pisa, Italy; CamGraPhiC, 56124 Pisa, Italy; Email: mromagnoli@cnit.it

Authors

Marco A. Giambra – Photonic Networks and Technologies Lab, CNIT, 56124 Pisa, Italy; INPHOTEC, 56124 Pisa, Italy; Center for Nanotechnology Innovation @NEST -

Istituto Italiano di Tecnologia, I-56127 Pisa, Italy;

orcid.org/0000-0002-1566-2395

Vaidotas Miseikis – Center for Nanotechnology Innovation @ NEST - Istituto Italiano di Tecnologia, I-56127 Pisa, Italy; Graphene Labs, Istituto Italiano di Tecnologia, 16163 Genova, Italy; orcid.org/0000-0001-6263-4250

Sergio Pezzini – Center for Nanotechnology Innovation @ NEST - Istituto Italiano di Tecnologia, I-56127 Pisa, Italy; Graphene Labs, Istituto Italiano di Tecnologia, 16163 Genova, Italy; NEST, Scuola Normale Superiore and Istituto Nanoscienze-CNR, I-56127 Pisa, Italy; orcid.org/0000-0003-4289-907X

Simone Marconi – Photonic Networks and Technologies Lab, Tecip Institute, Scuola Superiore Sant'Anna, 56124 Pisa, Italy

Alberto Montanaro – Photonic Networks and Technologies Lab, CNIT, 56124 Pisa, Italy

Filippo Fabbri – Center for Nanotechnology Innovation @ NEST - Istituto Italiano di Tecnologia, I-56127 Pisa, Italy; Graphene Labs, Istituto Italiano di Tecnologia, 16163 Genova, Italy; NEST, Scuola Normale Superiore and Istituto Nanoscienze-CNR, I-56127 Pisa, Italy; orcid.org/0000-0003-1142-0441

Vito Sorianello – Photonic Networks and Technologies Lab, CNIT, 56124 Pisa, Italy

Andrea C. Ferrari – Cambridge Graphene Centre, Cambridge University, Cambridge, U.K.; orcid.org/0000-0003-0907-9993

Complete contact information is available at:

<https://pubs.acs.org/10.1021/acsnano.0c09758>

Author Contributions

[†]M.A.G. and V.M. contributed equally to this work.

Author Contributions

[‡]C.C. and M.R. are joint last coauthors.

Notes

The authors declare no competing financial interest.

ACKNOWLEDGMENTS

We acknowledge funding from the European Union H2020 Graphene Flagship under grant agreements nos. 785219 and 881603, ERC grants Hetero2D, GSYNCOR, EPSRC grants EP/L016087/1, EP/K01711X/1, EP/K017144/1, EP/N010345/1.

REFERENCES

- (1) Bonaccorso, F.; Sun, Z.; Hasan, T.; Ferrari, A. C. Graphene Photonics and Optoelectronics. *Nat. Photonics* **2010**, *4*, 611–622.
- (2) Romagnoli, M.; Sorianello, V.; Midrio, M.; Koppens, F. H. L.; Huyghebaert, C.; Neumaier, D.; Galli, P.; Templ, W.; D'Errico, A.; Ferrari, A. C. Graphene-Based Integrated Photonics for Next-Generation Datacom and Telecom. *Nat. Rev. Mater.* **2018**, *3*, 392–414.
- (3) Koppens, F. H. L.; Mueller, T.; Avouris, P.; Ferrari, A. C.; Vitiello, M. S.; Polini, M. Photodetectors Based on Graphene, Other Two-Dimensional Materials and Hybrid Systems. *Nat. Nanotechnol.* **2014**, *9*, 780–793.
- (4) Ferrari, A. C.; Bonaccorso, F.; Fal'ko, V.; Novoselov, K. S.; Roche, S.; Boggild, P.; Borini, S.; Koppens, F. H. L.; Palermo, V.; Pugno, N.; Garrido, J. A.; Sordan, R.; Bianco, A.; Ballerini, L.; Prato, M.; Lidorikis, E.; Kivioja, J.; Marinelli, C.; Ryhänen, T.; Morpurgo, A.; et al. Science and Technology Roadmap for Graphene, Related Two-

- Dimensional Crystals, and Hybrid Systems. *Nanoscale* **2015**, *7*, 4598–4810.
- (5) Romagnoli, M. Graphene Photonics for Optical Communications. In *Optical Fiber Communication Conference (OFC)*; OSA: Washington, DC, 2019; p M3D.3.
- (6) Romagnoli, M. Graphene Photonics for Optical Communications. In *Broadband Access Communication Technologies XIII*; Dingel, B. B., Tsukamoto, K., Mikroulis, S., Eds.; SPIE, 2019; p 1.
- (7) Cisco. Cisco Annual Internet Report (2018–2023). <https://www.cisco.com/c/en/us/solutions/collateral/executive-perspectives/annual-internet-report/white-paper-c11-741490.pdf> (accessed 2020-03-09).
- (8) Evans, D. The Internet of Things How the Next Evolution of the Internet Is Changing Everything. https://www.cisco.com/c/dam/en_us/about/ac79/docs/innov/IoT_IBSG_0411FINAL.pdf (accessed 2011-04).
- (9) International Telecommunication Union. Definitions of World Telecommunication/Ict Indicators. https://www.itu.int/ITU-D/ict/material/TelecomICT_Indicators_Definition_March2010_for_web.pdf (accessed 2010-03).
- (10) Next Generation Mobile Networks Alliance. Next Generation Mobile 5G White Paper. https://www.ngmn.org/wp-content/uploads/NGMN_5G_White_Paper_V1_0.pdf (accessed 2015-02-17).
- (11) Ericsson Mobility Report. Available at: <https://www.ericsson.com/49da93/assets/local/mobility-report/documents/2020/june2020-ericsson-mobility-report.pdf> (accessed 2020-03).
- (12) How the Internet Can Cope with the Explosion of Demand for “Right Now” Data during the Coronavirus Outbreak <https://spectrum.ieee.org/tech-talk/telecom/internet/everyone-staying-home-because-of-covid19-is-targeting-the-internets-biggest-weak-spot> (accessed 2020-03-23).
- (13) 2020 Ethernet Roadmap <https://ethernetalliance.org/technology/2020-roadmap/> (accessed 2020-02-14).
- (14) Doerr, C. R. Silicon Photonic Integration in Telecommunications. *Front. Phys.* **2015**, *3*, 3.
- (15) Marchetti, R.; Lacava, C.; Carroll, L.; Gradkowski, K.; Minzioni, P. Coupling Strategies for Silicon Photonics Integrated Chips. *Photonics Res.* **2019**, *7*, 201.
- (16) Selvaraja, S. K.; De Heyn, P.; Winroth, G.; Ong, P.; Lepage, G.; Cailler, C.; Rigny, A.; Bourdelle, K. K.; Bogaerts, W.; Van Thourhout, D.; Van Campenhout, J.; Absil, P. Highly Uniform and Low-Loss Passive Silicon Photonics Devices Using a 300mm CMOS Platform. In *Optical Fiber Communication Conference*; OSA: Washington, DC, 2014; p Th2A.33.
- (17) Yariv, A.; Yeh, P. Photonics: Optical Electronics in Modern Communications; *Oxford series in electrical and computer engineering*; Oxford University Press: New York, 2007.
- (18) PSM4MSAGroup. 100G PSM4MSA Specification. <http://psm4.org/100G-PSM4-Specification-2.0.pdf> (accessed 2014-09-15).
- (19) Petrilla, J.; Cole, C.; King, J.; Lewis, D.; Hiramoto, K.; Tsumura, E. 100G CWDM4MSA Specifications. http://www.cwdm4msa.org/files/CWDM4_MSA_Technical_Spec_1p0.pdf (accessed 2014-08-27).
- (20) Miller, D. Device Requirements for Optical Interconnects to Silicon Chips. *Proc. IEEE* **2009**, *97*, 1166–1185.
- (21) Yoo, S. J. B. The Role of Photonics in Future Computing and Data Centers. *IEICE Trans. Commun.* **2014**, *E97.B*, 1272–1280.
- (22) Tekin, T.; Pleros, N.; Pitwon, R.; Hakansson, A. *Optical Interconnects for Data Centers*; Woodhead Publishing: Cambridge, 2016.
- (23) Colinge, J.-P. *Silicon-on-Insulator Technology: Materials to VLSI*; Springer-Verlag: New York, 2004.
- (24) Letal, G.; Prosyk, K.; Millett, R.; Macquistan, D.; Paquet, S.; Thibault-Maheu, O.; Gagné, J.; Fortin, P.; Dowlatshahi, R.; Rioux, B.; SpringThorpe, T.; Hisko, M.; Ma, R.; Woods, I. Low Loss InP C-Band IQ Modulator with 40 GHz Bandwidth and 1.5V V_{π} . In *2015 Optical Fiber Communications Conference and Exhibition (OFC) 2015*, 1–3.
- (25) Doerr, C.; Chen, L. Silicon Photonics in Optical Coherent Systems. *Proc. IEEE* **2018**, *106*, 2291–2301.
- (26) Witzens, J. High-Speed Silicon Photonics Modulators. *Proc. IEEE* **2018**, *106*, 2158–2182.
- (27) Valdar, A.; Morfett, I. *Understanding Telecommunications Business; Telecommunications*; Institution of Engineering and Technology: Stevenage, UK, 2015.
- (28) Tong, Y.; Hu, Z.; Wu, X.; Liu, S.; Chang, L.; Netherton, A.; Chan, C.-K.; Bowers, J. E.; Tsang, H. K. An Experimental Demonstration of 160-Gbit/s PAM-4 Using a Silicon Micro-Ring Modulator. *IEEE Photonics Technol. Lett.* **2020**, *32*, 125–128.
- (29) Verbist, J.; Verplaetse, M.; Srinivasan, S. A.; Van Kerrebrouck, J.; De Heyn, P.; Absil, P.; De Keulenaer, T.; Pierco, R.; Vyncke, A.; Torfs, G.; Yin, X.; Roelkens, G.; Van Campenhout, J.; Bauwelinck, J. Real-Time 100 Gb/s NRZ and EDB Transmission with a GeSi Electroabsorption Modulator for Short-Reach Optical Interconnects. *J. Lightwave Technol.* **2018**, *36*, 90–96.
- (30) Wang, B.; Huang, Q.; Chen, K.; Zhang, J.; Kurczveil, G.; Liang, D.; Palermo, S.; Tan, M. R. T.; Beausoleil, R. G.; He, S. Modulation on Silicon for Datacom: Past, Present, And Future (Invited Review). *Prog. Electromagn. Res.* **2019**, *166*, 119–145.
- (31) Smit, M.; Williams, K.; van der Tol, J. Past, Present, and Future of InP-Based Photonic Integration. *APL Photonics* **2019**, *4*, 050901.
- (32) Yole Développement. Silicon Photonics and Photonic Integrated Circuits 2019 by Yole Développement. https://www.slideshare.net/Yole_Developpement/silicon-photonics-and-photonic-integrated-circuits-2019-by-yole-dveloppement (accessed 2019-04-25).
- (33) Comparison between InP and Silicon Photonics. <https://www.phiconference.com/market/comparison-between-inp-and-silicon-photonics/> (accessed 2015-06-17).
- (34) Soriano, V.; Midrio, M.; Romagnoli, M. Design Optimization of Single and Double Layer Graphene Phase Modulators in SOI. *Opt. Express* **2015**, *23*, 6478.
- (35) Banszerus, L.; Schmitz, M.; Engels, S.; Dauber, J.; Oellers, M.; Haupt, F.; Watanabe, K.; Taniguchi, T.; Beschoten, B.; Stampfer, C. Ultrahigh-Mobility Graphene Devices from Chemical Vapor Deposition on Reusable Copper. *Sci. Adv.* **2015**, *1*, No. e1500222.
- (36) Purdie, D. G.; Pugno, N. M.; Taniguchi, T.; Watanabe, K.; Ferrari, A. C.; Lombardo, A. Cleaning Interfaces in Layered Materials Heterostructures. *Nat. Commun.* **2018**, *9*, 5387.
- (37) De Fazio, D.; Purdie, D. G.; Ott, A. K.; Braeuninger-Weimer, P.; Khodkov, T.; Goossens, S.; Taniguchi, T.; Watanabe, K.; Livreri, P.; Koppens, F. H. L.; Hofmann, S.; Goykhman, I.; Ferrari, A. C.; Lombardo, A. High-Mobility, Wet-Transferred Graphene Grown by Chemical Vapor Deposition. *ACS Nano* **2019**, *13*, 8926–8935.
- (38) Pezzini, S.; Mišeikis, V.; Pace, S.; Rossella, F.; Watanabe, K.; Taniguchi, T.; Coletti, C. High-Quality Electrical Transport Using Scalable CVD Graphene. *2D Mater.* **2020**, *7*, 041003.
- (39) Banszerus, L.; Sohler, T.; Epping, A.; Winkler, F.; Libisch, F.; Haupt, F.; Watanabe, K.; Taniguchi, T.; Müller-Caspary, K.; Marzari, N.; Mauri, F.; Beschoten, B.; Stampfer, C. Extraordinary High Room-Temperature Carrier Mobility in Graphene-WSe₂ Heterostructures. *arXiv:1909.09523* <https://arxiv.org/abs/1909.09523> (accessed 2020-05-12).
- (40) Banszerus, L.; Schmitz, M.; Engels, S.; Goldsche, M.; Watanabe, K.; Taniguchi, T.; Beschoten, B.; Stampfer, C. Ballistic Transport Exceeding 28 Mm in CVD Grown Graphene. *Nano Lett.* **2016**, *16*, 1387–1391.
- (41) Novoselov, K. S.; Geim, A. K.; Morozov, S. V.; Jiang, D.; Zhang, Y.; Dubonos, S. V.; Grigorieva, I. V.; Firsov, A. A. Electric Field Effect in Atomically Thin Carbon Films. *Science* **2004**, *306*, 666.
- (42) Wang, F.; Zhang, Y.; Tian, C.; Girit, C.; Zettl, A.; Crommie, M.; Shen, Y. R. Gate-Variable Optical Transitions in Graphene. *Science* **2008**, *320*, 206–209.
- (43) Stauber, T.; Peres, N. M. R.; Geim, A. K. Optical Conductivity of Graphene in the Visible Region of the Spectrum. *Phys. Rev. B: Condens. Matter Mater. Phys.* **2008**, *78*, 085432.

- (44) Li, H.; Anugrah, Y.; Koester, S. J.; Li, M. Optical Absorption in Graphene Integrated on Silicon Waveguides. *Appl. Phys. Lett.* **2012**, *101*, 111110.
- (45) Liu, M.; Yin, X.; Zhang, X. Double-Layer Graphene Optical Modulator. *Nano Lett.* **2012**, *12*, 1482–1485.
- (46) Liu, M.; Yin, X.; Ulin-Avila, E.; Geng, B.; Zentgraf, T.; Ju, L.; Wang, F.; Zhang, X. A Graphene-Based Broadband Optical Modulator. *Nature* **2011**, *474*, 64–67.
- (47) Giambra, M. A.; Soriano, V.; Miseikis, V.; Marconi, S.; Montanaro, A.; Galli, P.; Pezzini, S.; Coletti, C.; Romagnoli, M. High-Speed Double Layer Graphene Electro-Absorption Modulator on SOI Waveguide. *Opt. Express* **2019**, *27*, 20145–20155.
- (48) Midrio, M.; Galli, P.; Romagnoli, M.; Kimerling, L. C.; Michel, J. Graphene-Based Optical Phase Modulation of Waveguide Transverse Electric Modes. *Photonics Res.* **2014**, *2*, A34.
- (49) Soriano, V.; Midrio, M.; Contestabile, G.; Asselberghs, I.; Van Campenhout, J.; Huyghebaert, C.; Goykhman, I.; Ott, A. K.; Ferrari, A. C.; Romagnoli, M. Graphene-Silicon Phase Modulators with Gigahertz Bandwidth. *Nat. Photonics* **2018**, *12*, 40–44.
- (50) Cassese, T.; Giambra, M. A.; Soriano, V.; De Angelis, G.; Midrio, M.; Pantouvakis, M.; Van Campenhout, J.; Asselberghs, I.; Huyghebaert, C.; D'Errico, A.; Romagnoli, M. Capacitive Actuation and Switching of Add-Drop Graphene-Silicon Micro-Ring Filters. *Photonics Res.* **2017**, *5*, 762.
- (51) Song, J. C. W. W. C. W.; Rudner, M. S. S.; Marcus, C. M. M.; Levitov, L. S. S. Hot Carrier Transport and Photocurrent Response in Graphene. *Nano Lett.* **2011**, *11*, 4688–4692.
- (52) Muench, J. E.; Ruocco, A.; Giambra, M. A.; Miseikis, V.; Zhang, D.; Wang, J.; Watson, H. F. Y.; Park, G. C.; Akhavan, S.; Soriano, V.; Midrio, M.; Tomadin, A.; Coletti, C.; Romagnoli, M.; Ferrari, A. C.; Goykhman, I. Waveguide-Integrated, Plasmonic Enhanced Graphene Photodetectors. *Nano Lett.* **2019**, *19*, 7632–7644.
- (53) Shiue, R.-J.; Gao, Y.; Wang, Y.; Peng, C.; Robertson, A. D.; Efetov, D. K.; Assefa, S.; Koppens, F. H. L.; Hone, J.; Englund, D. High-Responsivity Graphene-Boron Nitride Photodetector and Autocorrelator in a Silicon Photonic Integrated Circuit. *Nano Lett.* **2015**, *15*, 7288–7293.
- (54) Mišeikis, V.; Marconi, S.; Giambra, M. A.; Montanaro, A.; Martini, L.; Fabbri, F.; Pezzini, S.; Piccinini, G.; Forti, S.; Terrés, B.; Goykhman, I.; Hamidouche, L.; Legagneux, P.; Soriano, V.; Ferrari, A. C.; Koppens, F. H. L.; Romagnoli, M.; Coletti, C. Ultrafast, Zero-Bias, Graphene Photodetectors with Polymeric Gate Dielectric on Passive Photonic Waveguides. *ACS Nano* **2020**, *14*, 11190–11204.
- (55) Marconi, S.; Giambra, M. A.; Montanaro, A.; Mišeikis, V.; Soresi, S.; Tirelli, S.; Galli, P.; Buchali, F.; Templ, W.; Coletti, C.; Soriano, V.; Romagnoli, M. Photo Thermal Effect Graphene Detector Featuring 105 Gbit s⁻¹ NRZ and 120 Gbit s⁻¹ PAM4 Direct Detection. *arXiv:2006.01481* <https://arxiv.org/abs/2006.01481> (accessed 2020-06-02).
- (56) Phare, C. T.; Daniel Lee, Y.-H.; Cardenas, J.; Lipson, M. Graphene Electro-Optic Modulator with 30 GHz Bandwidth. *Nat. Photonics* **2015**, *9*, 511–514.
- (57) Jalali, B.; Fathpour, S. Silicon Photonics. *J. Lightwave Technol.* **2006**, *24*, 4600–4615.
- (58) Dakin, J. P.; Brown, R. G. W. *Handbook of Optoelectronics*; CRC Press: Boca Raton, 2017.
- (59) Agrawal, G. P. *Lightwave Technology: Components and Devices*; John Wiley & Sons: New York, 2004.
- (60) Chrostowski, L.; Hochberg, M. *Silicon Photonics Design: From Devices to Systems*; Cambridge University Press: Cambridge, 2015.
- (61) Li, H. H. Refractive Index of Silicon and Germanium and Its Wavelength and Temperature Derivatives. *J. Phys. Chem. Ref. Data* **1980**, *9*, 561–658.
- (62) Horizon 2020 - Work Programme 2016 - 2017. https://ec.europa.eu/research/participants/data/ref/h2020/other/wp/2016-2017/annexes/h2020-wp1617-annex-ga_en.pdf (accessed 2017-04-24).
- (63) Petrone, N.; Dean, C. R.; Meric, I.; van der Zande, A. M.; Huang, P. Y.; Wang, L.; Muller, D.; Shepard, K. L.; Hone, J. Chemical Vapor Deposition-Derived Graphene with Electrical Performance of Exfoliated Graphene. *Nano Lett.* **2012**, *12*, 2751.
- (64) Chen, X.; Wu, B.; Liu, Y. Direct Preparation of High Quality Graphene on Dielectric Substrates. *Chem. Soc. Rev.* **2016**, *45*, 2057–2074.
- (65) Mishra, N.; Forti, S.; Fabbri, F.; Martini, L.; McAleese, C.; Conran, B. R. R.; Whelan, P. R. R.; Shivayogimath, A.; Jessen, B. S. S.; Buß, L.; Falta, J.; Aliaj, I.; Roddaro, S.; Flege, J. I. I.; Bøggild, P.; Teo, K. B. K. B. K.; Coletti, C. Wafer-Scale Synthesis of Graphene on Sapphire: Toward Fab-Compatible Graphene. *Small* **2019**, *15*, 1904906.
- (66) Lee, J.-H.; Lee, E. K.; Joo, W.-J.; Jang, Y.; Kim, B.-S.; Lim, J. Y.; Choi, S.-H.; Ahn, S. J.; Ahn, J. R.; Park, M.-H.; Yang, C.-W.; Choi, B. L.; Hwang, S.-W.; Whang, D. Wafer-Scale Growth of Single-Crystal Monolayer Graphene on Reusable Hydrogen-Terminated Germanium. *Science* **2014**, *344*, 286–289.
- (67) Lukosius, M.; Dabrowski, J.; Kitzmann, J.; Fursenko, O.; Akhtar, F.; Lisker, M.; Lippert, G.; Schulze, S.; Yamamoto, Y.; Schubert, M. A.; Krause, H. M.; Wolff, A.; Mai, A.; Schroeder, T.; Lupina, G. Metal-Free CVD Graphene Synthesis on 200 mm Ge/Si(001) Substrates. *ACS Appl. Mater. Interfaces* **2016**, *8*, 33786–33793.
- (68) Scaparro, A. M.; Miseikis, V.; Coletti, C.; Notargiacomo, A.; Pea, M.; De Seta, M.; Di Gaspare, L. Investigating the CVD Synthesis of Graphene on Ge(100): Toward Layer-by-Layer Growth. *ACS Appl. Mater. Interfaces* **2016**, *8*, 33083–33090.
- (69) Li, X.; Cai, W.; An, J.; Kim, S.; Nah, J.; Yang, D.; Piner, R.; Velamakanni, A.; Jung, I.; Tutuc, E.; Banerjee, S. K.; Colombo, L.; Ruoff, R. S. Large-Area Synthesis of High-Quality and Uniform Graphene Films on Copper Foils. *Science* **2009**, *324*, 1312–1314.
- (70) Bonaccorso, F.; Lombardo, A.; Hasan, T.; Sun, Z.; Colombo, L.; Ferrari, A. C. Production and Processing of Graphene and 2D Crystals. *Mater. Today* **2012**, *15*, 564–589.
- (71) Backes, C.; Abdelkader, A. M.; Alonso, C.; Andrieux-Ledier, A.; Arenal, R.; Azpeitia, J.; Balakrishnan, N.; Banszerus, L.; Barjon, J.; Bartali, R.; Bellani, S.; Berger, C.; Berger, R.; Ortega, M. M. B.; Bernard, C.; Beton, P. H.; Beyer, A.; Bianco, A.; Bøggild, P.; Bonaccorso, F.; et al. Production and Processing of Graphene and Related Materials. *2D Mater.* **2020**, *7*, 022001.
- (72) Reina, A.; Jia, X.; Ho, J.; Nezich, D.; Son, H.; Bulovic, V.; Dresselhaus, M. S.; Kong, J. Large Area, Few-Layer Graphene Films on Arbitrary Substrates by Chemical Vapor Deposition. *Nano Lett.* **2009**, *9*, 30–35.
- (73) Wang, Y.; Zheng, Y.; Xu, X.; Dubuisson, E.; Bao, Q.; Lu, J.; Loh, K. P. Electrochemical Delamination of CVD-Grown Graphene Film: Toward the Recyclable Use of Copper Catalyst. *ACS Nano* **2011**, *5*, 9927–9933.
- (74) Gao, L.; Ren, W.; Xu, H.; Jin, L.; Wang, Z.; Ma, T.; Ma, L.-P.; Zhang, Z.; Fu, Q.; Peng, L.-M.; Bao, X.; Cheng, H.-M. Repeated Growth and Bubbling Transfer of Graphene with Millimetre-Size Single-Crystal Grains Using Platinum. *Nat. Commun.* **2012**, *3*, 699.
- (75) Wang, R.; Whelan, P. R.; Braeuninger-Weimer, P.; Tappertzhofen, S.; Alexander-Webber, J. A.; Van Veldhoven, Z. A.; Kidambi, P. R.; Jessen, B. S.; Booth, T.; Bøggild, P.; Hofmann, S. Catalyst Interface Engineering for Improved 2D Film Lift-Off and Transfer. *ACS Appl. Mater. Interfaces* **2016**, *8*, 33072–33082.
- (76) Mišeikis, V.; Bianco, F.; David, J.; Gemmi, M.; Pellegrini, V.; Romagnoli, M.; Coletti, C. Deterministic Patterned Growth of High-Mobility Large-Crystal Graphene: A Path towards Wafer Scale Integration. *2D Mater.* **2017**, *4*, 021004.
- (77) Sonntag, J.; Li, J.; Plaud, A.; Loiseau, A.; Barjon, J.; Edgar, J. H.; Stampfer, C. Excellent Electronic Transport in Heterostructures of Graphene and Monoisotopic Boron-Nitride Grown at Atmospheric Pressure. *2D Mater.* **2020**, *7*, 031009.
- (78) Shivayogimath, A.; Whelan, P. R.; Mackenzie, D. M. A.; Luo, B.; Huang, D.; Luo, D.; Wang, M.; Gammelgaard, L.; Shi, H.; Ruoff, R. S.; Bøggild, P.; Booth, T. J. Do-It-Yourself Transfer of Large-Area Graphene Using an Office Laminator and Water. *Chem. Mater.* **2019**, *31*, 2328–2336.

- (79) Miseikis, V.; Convertino, D.; Mishra, N.; Gemmi, M.; Mashoff, T.; Heun, S.; Haghghian, N.; Bisio, F.; Canepa, M.; Piazza, V.; Coletti, C. Rapid CVD Growth of Millimetre-Sized Single Crystal Graphene Using a Cold-Wall Reactor. *2D Mater.* **2015**, *2*, 014006.
- (80) Alexander, K.; George, J. P.; Verbist, J.; Neyts, K.; Kuyken, B.; Van Thourhout, D.; Beeckman, J. Nanophotonic Pockels Modulators on a Silicon Nitride Platform. *Nat. Commun.* **2018**, *9*, 3444.
- (81) Zurrón, Ó.; Picón, A.; Plaja, L. Theory of High-Order Harmonic Generation for Gapless Graphene. *New J. Phys.* **2018**, *20*, 053033.
- (82) Mohsin, M.; Schall, D.; Otto, M.; Nocolak, A.; Neumaier, D.; Kurz, H. Graphene Based Low Insertion Loss Electro-Absorption Modulator on SOI Waveguide. *Opt. Express* **2014**, *22*, 15292.
- (83) Hao, Y.; Bharathi, M. S.; Wang, L.; Liu, Y.; Chen, H.; Nie, S.; Wang, X.; Chou, H.; Tan, C.; Fallahzad, B.; Ramanarayan, H.; Magnuson, C. W.; Tutuc, E.; Yakobson, B. L.; McCarty, K. F.; Zhang, Y.-W.; Kim, P.; Hone, J.; Colombo, L.; Ruoff, R. S. The Role of Surface Oxygen in the Growth of Large Single-Crystal Graphene on Copper. *Science* **2013**, *342*, 720–723.
- (84) Kang, S. J.; Kim, B.; Kim, K. S.; Zhao, Y.; Chen, Z.; Lee, G. H.; Hone, J.; Kim, P.; Nuckolls, C. Inking Elastomeric Stamps with Micro-Patterned, Single Layer Graphene to Create High-Performance OFETs. *Adv. Mater.* **2011**, *23*, 3531–3535.
- (85) SYLGARD™ 184 Silicone Elastomer Kit Technical Data Sheet. <https://www.dow.com/en-us/document-viewer.html?randomVar=577327118110380375&docPath=/content/dam/dcc/documents/en-us/productdatasheet/11/11-31/11-3184-sylgard-184-elastomer.pdf> (accessed 2019-05-18).
- (86) Polymer Properties Database <http://polymerdatabase.com/polymerphysics/PolymerTgC.html>.
- (87) Gao, L.; Ni, G.-X.; Liu, Y.; Liu, B.; Castro Neto, A. H.; Loh, K. P. Face-to-Face Transfer of Wafer-Scale Graphene Films. *Nature* **2014**, *505*, 190–194.
- (88) Kim, M.; Shah, A.; Li, C.; Mustonen, P.; Susoma, J.; Manoocheri, F.; Riikonen, J.; Lipsanen, H. Direct Transfer of Wafer-Scale Graphene Films. *2D Mater.* **2017**, *4*, 035004.
- (89) Zhu, W.; Neumayer, D.; Perebeinos, V.; Avouris, P. Silicon Nitride Gate Dielectrics and Band Gap Engineering in Graphene Layers. *Nano Lett.* **2010**, *10*, 3572–3576.
- (90) Khosrofiyan, J. M.; Garetz, B. A. Measurement of a Gaussian Laser Beam Diameter through the Direct Inversion of Knife-Edge Data. *Appl. Opt.* **1983**, *22*, 3406.
- (91) Dwivedi, N.; Ott, A. K.; Sasikumar, K.; Dou, C.; Yeo, R. J.; Narayanan, B.; Sassi, U.; De Fazio, D.; Soavi, G.; Dutta, T.; Sarakanarayanan, S. K. R. S.; Ferrari, A. C.; Bhatia, C. S. Graphene Overcoats for Ultra-High Storage Density Magnetic Media. *arXiv:1906.00338*, <https://arxiv.org/abs/1906.00338> (accessed 2020-05-12).
- (92) Single Layer h-BN (Boron Nitride) Film Grown on Copper Foil: 2" x 1 <https://graphene-supermarket.com/Single-layer-h-BN-Boron-Nitride-film-grown-in-copper-foil-2-x-1.html> (accessed 2020-06-15).
- (93) Ferrari, A. C.; Meyer, J. C.; Scardaci, V.; Casiraghi, C.; Lazzeri, M.; Mauri, F.; Piscanec, S.; Jiang, D.; Novoselov, K. S.; Roth, S.; Geim, A. K. Raman Spectrum of Graphene and Graphene Layers. *Phys. Rev. Lett.* **2006**, *97*, 187401.
- (94) Ferrari, A. C.; Basko, D. M. Raman Spectroscopy as a Versatile Tool for Studying the Properties of Graphene. *Nat. Nanotechnol.* **2013**, *8*, 235–246.
- (95) Cañado, L. G.; Jorio, A.; Ferreira, E. H. M.; Stavale, F.; Achete, C. A.; Capaz, R. B.; Moutinho, M. V. O.; Lombardo, A.; Kulmala, T. S.; Ferrari, A. C. Quantifying Defects in Graphene via Raman Spectroscopy at Different Excitation Energies. *Nano Lett.* **2011**, *11*, 3190.
- (96) Ni, Z. H.; Ponomarenko, L. A.; Nair, R. R.; Yang, R.; Anissimova, S.; Grigorieva, I. V.; Schedin, F.; Blake, P.; Shen, Z. X.; Hill, E. H.; Novoselov, K. S.; Geim, A. K. On Resonant Scatterers as a Factor Limiting Carrier Mobility in Graphene. *Nano Lett.* **2010**, *10*, 3868–3872.
- (97) Chen, J.-H.; Cullen, W. G.; Jang, C.; Fuhrer, M. S.; Williams, E. D. Defect Scattering in Graphene. *Phys. Rev. Lett.* **2009**, *102*, 236805.
- (98) Casiraghi, C.; Pisana, S.; Novoselov, K. S.; Geim, A. K.; Ferrari, A. C. Raman Fingerprint of Charged Impurities in Graphene. *Appl. Phys. Lett.* **2007**, *91*, 233108.
- (99) Das, A.; Pisana, S.; Chakraborty, B.; Piscanec, S.; Saha, S. K.; Waghmare, U. V.; Novoselov, K. S.; Krishnamurthy, H. R.; Geim, A. K.; Ferrari, A. C.; Sood, A. K. Monitoring Dopants by Raman Scattering in an Electrochemically Top-Gated Graphene Transistor. *Nat. Nanotechnol.* **2008**, *3*, 210–215.
- (100) Basko, D. M.; Piscanec, S.; Ferrari, A. C. Electron-Electron Interactions and Doping Dependence of the Two-Phonon Raman Intensity in Graphene. *Phys. Rev. B: Condens. Matter Mater. Phys.* **2009**, *80*, 165413.
- (101) Bruna, M.; Ott, A. K.; Ijäs, M.; Yoon, D.; Sassi, U.; Ferrari, A. C. Doping Dependence of the Raman Spectrum of Defected Graphene. *ACS Nano* **2014**, *8*, 7432–7441.
- (102) Mohiuddin, T. M. G.; Lombardo, A.; Nair, R. R.; Bonetti, A.; Savini, G.; Jalil, R.; Bonini, N.; Basko, D. M.; Galotis, C.; Marzari, N.; Novoselov, K. S.; Geim, A. K.; Ferrari, A. C. Uniaxial Strain in Graphene by Raman Spectroscopy: G Peak Splitting, Grüneisen Parameters, and Sample Orientation. *Phys. Rev. B: Condens. Matter Mater. Phys.* **2009**, *79*, 205433.
- (103) Yoon, D.; Son, Y. W.; Cheong, H. Strain-Dependent Splitting of the Double-Resonance Raman Scattering Band in Graphene. *Phys. Rev. Lett.* **2011**, *106*, 155502.
- (104) Zabel, J.; Nair, R. R.; Ott, A.; Georgiou, T.; Geim, A. K.; Novoselov, K. S.; Casiraghi, C. Raman Spectroscopy of Graphene and Bilayer under Biaxial Strain: Bubbles and Balloons. *Nano Lett.* **2012**, *12*, 617–621.
- (105) Piscanec, S.; Lazzeri, M.; Mauri, F.; Ferrari, A. C.; Robertson, J. Kohn Anomalies and Electron-Phonon Interactions in Graphite. *Phys. Rev. Lett.* **2004**, *93*, 1–4.
- (106) Pisana, S.; Lazzeri, M.; Casiraghi, C.; Novoselov, K. S.; Geim, A. K.; Ferrari, A. C.; Mauri, F. Breakdown of the Adiabatic Born-Oppenheimer Approximation in Graphene. *Nat. Mater.* **2007**, *6*, 198–201.
- (107) Tran, T. T.; Bray, K.; Ford, M. J.; Toth, M.; Aharonovich, I. Quantum Emission from Hexagonal Boron Nitride Monolayers. *Nat. Nanotechnol.* **2016**, *11*, 37–41.
- (108) Lee, J. E.; Ahn, G.; Shim, J.; Lee, Y. S.; Ryu, S. Optical Separation of Mechanical Strain from Charge Doping in Graphene. *Nat. Commun.* **2012**, *3*, 1024.
- (109) Neumann, C.; Reichardt, S.; Venezuela, P.; Drögeler, M.; Banzerus, L.; Schmitz, M.; Watanabe, K.; Taniguchi, T.; Mauri, F.; Beschoten, B.; Rotkin, S. V.; Stampfer, C. Raman Spectroscopy as Probe of Nanometre-Scale Strain Variations in Graphene. *Nat. Commun.* **2015**, *6*, 8429.
- (110) Couto, N. J. G.; Costanzo, D.; Engels, S.; Ki, D.-K.; Watanabe, K.; Taniguchi, T.; Stampfer, C.; Guinea, F.; Morpurgo, A. F. Random Strain Fluctuations as Dominant Disorder Source for High-Quality On-Substrate Graphene Devices. *Phys. Rev. X* **2014**, *4*, 041019.
- (111) Berger, H. H. Models for Contacts to Planar Devices. *Solid-State Electron.* **1972**, *15*, 145–158.
- (112) Wang, L.; Meric, I.; Huang, P. Y.; Gao, Q.; Gao, Y.; Tran, H.; Taniguchi, T.; Watanabe, K.; Campos, L. M.; Muller, D. A.; Guo, J.; Kim, P.; Hone, J.; Shepard, K. L.; Dean, C. R. One-Dimensional Electrical Contact to a Two-Dimensional Material. *Science* **2013**, *342*, 614–617.
- (113) Falkovsky, L. A. Optical Properties of Graphene. *J. Phys. Conf. Ser.* **2008**, *129*, 012004.
- (114) Kim, S.; Nah, J.; Jo, I.; Shahrjerdi, D.; Colombo, L.; Yao, Z.; Tutuc, E.; Banerjee, S. K. Realization of a High Mobility Dual-Gated Graphene Field-Effect Transistor with Al₂O₃ Dielectric. *Appl. Phys. Lett.* **2009**, *94*, 062107.
- (115) Huard, B.; Stander, N.; Sulpizio, J. A.; Goldhaber-Gordon, D. Evidence of the Role of Contacts on the Observed Electron-Hole Asymmetry in Graphene. *Phys. Rev. B: Condens. Matter Mater. Phys.* **2008**, *78*, 121402.

- (116) Lee, E. J.; Balasubramanian, K.; Weitz, R. T.; BurkHard, M.; Kern, K. Contact and Edge Effects in Graphene Devices. *Nat. Nanotechnol.* **2008**, *3*, 486–490.
- (117) Valdes, L. Resistivity Measurements on Germanium for Transistors. *Proc. IRE* **1954**, *42*, 420–427.
- (118) Hanson, G. W. Dyadic Green's Functions and Guided Surface Waves for a Surface Conductivity Model of Graphene. *J. Appl. Phys.* **2008**, *103*, 064302.
- (119) Alexander, C. K.; Sadiku, M. *Fundamentals of Electric Circuits*; McGraw-Hill: London, UK, 2008.
- (120) Xia, J.; Chen, F.; Li, J.; Tao, N. Measurement of the Quantum Capacitance of Graphene. *Nat. Nanotechnol.* **2009**, *4*, 505–509.
- (121) Razavi, B. *Design of Integrated Circuits for Optical Communications*; John Wiley & Sons: New York, NY, 2012.
- (122) Pitris, S.; Moralis-Pegios, M.; Alexoudi, T.; Fotiadis, K.; Ban, Y.; Heyn, P.; De Campenhout, J.; Van Pleros, N. A 400 Gb/s O-Band WDM (8×50 Gb/s) Silicon Photonic Ring Modulator-Based Transceiver. In *2020 Optical Fiber Communications Conference and Exhibition (OFC) 2020*, 1–3.
- (123) Chaisakul, P.; Vakarin, V.; Frigerio, J.; Chrastina, D.; Isella, G.; Vivien, L.; Marris-Morini, D. Recent Progress on Ge/SiGe Quantum Well Optical Modulators, Detectors, and Emitters for Optical Interconnects. *Photonics* **2019**, *6*, 24.
- (124) Heebner, J.; Grover, R.; Ibrahim, T. *Optical Microresonators*; Springer-Verlag: New York, 2008.
- (125) Kim, K. K.; Hsu, A.; Jia, X.; Kim, S. M.; Shi, Y.; Hofmann, M.; Nezich, D.; Rodriguez-Nieva, J. F.; Dresselhaus, M.; Palacios, T.; Kong, J. Synthesis of Monolayer Hexagonal Boron Nitride on Cu Foil Using Chemical Vapor Deposition. *Nano Lett.* **2012**, *12*, 161–166.